A Further Study of the Tropical Western Hemisphere Warm Pool

By

Chunzai Wang

and

David B. Enfield

NOAA Atlantic Oceanographic and Meteorological Laboratory

Miami, Florida

Journal of Climate

October 31, 2002

Corresponding author address: Dr. Chunzai Wang, NOAA/AOML, Physical Oceanography Division, 4301 Rickenbacker Causeway, Miami, FL 33149. E-mail: Chunzai.Wang@noaa.gov.

Abstract

Variability of the tropical Western Hemisphere warm pool (WHWP) of water warmer than 28.5°C, which extends seasonally over parts of the eastern North Pacific, the Gulf of Mexico, the Caribbean, and the western tropical North Atlantic (TNA), is previously studied by Wang and Enfield using the da Silva data from 1945-1993. Using additional data sets of the NCEP-NCAR reanalysis field and the NCEP SST from 1950-1999, and the Levitus climatological subsurface temperature, the present paper confirms and extends the previous study of Wang and Enfield. The WHWP alternates with northern South America as the seasonal heating source for the Walker and Hadley circulations in the Western Hemisphere. During the boreal winter a strong Hadley cell emanates northward from the Amazon heat source with subsidence over the subtropical North Atlantic north of 20°N, sustaining a strong North Atlantic anticyclone and associated northeast (NE) trade winds over its southern limb in the TNA. This circulation, including the NE trades, is weakened during Pacific El Niño winters and results in a spring warming of the TNA, which in turn induces the development of an unusually large summer warm pool and a wetter Caribbean rainy season. As the WHWP develops in the late boreal spring, the center of tropospheric heating and convection shifts to the WHWP region, whence the summer Hadley circulation emanates from the WHWP and forks into the subsidence regions of the subtropical South Atlantic and South Pacific. During the summers following El Niño, when the warm pool is larger than normal, the increased Hadley flow into the subtropical South Pacific reinforces the South Pacific anticyclone and trade winds, probably playing a role in the transition back to the cool phase of ENSO.

Seasonally, surface heat fluxes seem to be primarily responsible for warming of the WHWP. Interannually, all of the data sets suggest that a positive ocean-atmosphere feedback through longwave radiation and associated cloudiness seems to operate in the WHWP. During winter preceding large warm pool, there is a strong weakening of the Hadley cell that serves as a "tropospheric bridge" for transferring El Niño effects to the Atlantic sector and inducing warming of warm pool. Associated with the warm SST anomalies is a decrease in sea level pressure anomalies and an anomalous increase in atmospheric convection and cloudiness. The increase in convective activity and cloudiness results in less longwave radiation loss from the sea surface, which then reinforces SST anomalies. This data-inferred hypothesis of the longwave radiation feedback process needs to be further investigated for its validation in the WHWP.

1. Introduction

Wang and Enfield (2001; hereinafter referred to as WE01) described and examined variability of the tropical Western Hemisphere warm pool (WHWP) by using the da Silva et al. (1994) data from January 1945 to December 1993. The WHWP was defined as the region covered by water warmer than 28.5°C. These are temperatures that have a significant impact on organized tropical convection (e.g., Graham and Barnett 1987). They usually disappear at the winter minimum and subtend a large but closed region during the summer maximum. Not only is the choice of 28.5°C based on limiting the WHWP to a closed region, it is also based on the fact that the depth of the 28.5°C isotherm is closest to the average mixed layer depth in the WHWP. Unlike the Eastern Hemisphere warm pool in the western Pacific (e.g., Webster and Lukas 1992), which straddles the equator, the WHWP is entirely north of the equator. At various stages of development, the WHWP is comprised of the eastern North Pacific (ENP) west of Central America, the Intra-Americas Sea (IAS), i.e., the Gulf of Mexico and the Caribbean, and the western tropical North Atlantic (TNA).

The adoption of a warm pool definition that includes two ocean regions (ENP and IAS) separated by the Central American landmass is based on our primary interest in the WHWP as an atmospheric heat source, and not as an oceanographic phenomenon. To the atmosphere, the WHWP is a monolithic heat source that annually migrates and changes in size (Wang 2002b), with little regard for the narrow landmass of Central America. We nevertheless recognize that WHWP development may involve oceanographic processes that are fundamentally different between the two oceans, and that these must be accounted for.

WE01 showed that the WHWP has a large seasonal cycle and the interannual fluctuations of its area are comparable to the annual variation. Surface heat fluxes warm the WHWP through the boreal spring to an annual maximum of sea surface temperature (SST) and areal extent in the late summer and early fall. Anomalies of SST intensity and WHWP area anomalies occur at high temperatures where small changes can have a large impact on tropical convection. The da Silva et al. (1994) data suggest that a positive ocean-atmosphere feedback operating through longwave

radiation and associated cloudiness may account for the persistence of the WHWP SST anomalies (WE01). The data showed that, associated with an increase in SST anomalies is a decrease in atmospheric sea level pressure (SLP) anomalies and an anomalous increase in atmospheric convection and cloudiness. The increase in convective activity and cloudiness results in less net longwave radiation loss from the sea surface, which then reinforces SST anomalies.

The present paper is an extension and a continuation of the investigation initiated in WE01, providing additional information about how warm pool anomalies may occur. The NCEP-NCAR (National Centers for Environmental Prediction-National Center for Atmospheric Research) reanalysis field and the NCEP SST from 1950-1999 are analyzed to re-examine the results of the WHWP seasonal and interannual variability concluded from the da Silva et al. (1994) data from 1945-1993. These independent data sets show similar results, suggesting that the seasonal and interannual variability of WE01 are robust features of the WHWP. Additionally, the present paper examines and discusses the tropospheric circulation patterns of the Walker and Hadley circulation cells associated with the WHWP, and a tropospheric bridge for transferring Pacific El Niño effects to the Atlantic sector. The Levitus climatological subsurface temperature (Levitus and Boyer 1994) is also analyzed to investigate three-dimensional variations of the WHWP. Section 2 introduces the data sets used in this paper. Section 3 shows annual variability of the WHWP. Section 4 shows interannual variability of the WHWP. Section 5 analyzes the role of longwave radiation in the WHWP. Section 6 provides a discussion and summary.

2. Data

WE01 described and examined seasonal and interannual variability of the WHWP, using the da Silva et al. (1994) data from January 1945 to December 1993. In the present paper, we use the NCEP-NCAR reanalysis field from January 1950 to December 1999 for atmospheric variables, the NCEP SST from January 1950 to December 1999, and the Levitus climatological subsurface temperature data. The NCEP-NCAR reanalysis field uses a state-of-the-art global data assimilation system on a 2.5° longitude by 2.5° latitude grid (Kalnay et al. 1996). Variables used in this study

are monthly SLP, surface heat flux, cloud cover, horizontal wind velocity, vertical velocity, and velocity potential. The horizontal wind velocity, vertical velocity, and velocity potential are at levels of 1000, 925, 850, 700, 600, 500, 400, 300, 250, 200, 150, and 100 hPa. The vertical component of wind field in the NCEP-NCAR reanalysis field is pressure vertical velocity. In our presentation, we multiply the pressure vertical velocity by –1, so positive values of the vertical velocity indicate an upward movement of air parcels.

Horizontal wind velocity can be divided into a nondivergent (or rotational) part and a divergent (or irrotational) part (e.g., Mancuso 1967; Krishnamurti 1971; Krishnamurti et al. 1973): $\vec{v} = \vec{v}_\psi + \vec{v}_\chi = \vec{k} \times \nabla\psi + \nabla\chi$, where ψ is streamfunction and χ is velocity potential. The first part does not contribute to atmospheric divergent fields associated with atmospheric vertical motion (it is nondivergent). It is well known that the Walker and Hadley cells are thermally driven, associated with geographical foci of atmospheric convergence and divergence. In the Tropics, atmospheric heating associated with convection induces atmospheric convergence and divergence that drive atmospheric vertical motion and circulation. This direct circulation, comprised of zonal (Walker) and meridional (Hadley) cells, is therefore best characterized by the divergent component of flow. In this paper, we will mainly focus on the distributions of atmospheric vertical motion and the divergent component of the wind when we discuss atmospheric circulation cells.

The NCEP SST data are monthly on a 2° latitude × 2° longitude grid from January 1950 to December 1999. These SST fields are an updated version of those originally produced by Smith et al. (1996) using a spatial interpolation method employing empirical orthogonal function (EOF) analysis. With the data sets, we first calculate monthly climatologies based on the full record period (1950-1999) and then anomalies are obtained by subtracting the monthly climatologies for each data set from the data. Two types of WHWP indices have been derived from the SST data set. One is an SST intensity index, which is simply the time series of monthly averaged SST or SST anomalies for a rectangular region of 7°N-27°N, 110°W-50°W. The other is the index of the

area enclosed by the 28.5°C isotherm (see WE01). The WHWP is also divided into the ENP and IAS components separated by the Central American landmass.

In this study, we also use the Levitus climatological depth-distributed ocean temperature and mixed layer depth (MLD) (Levitus and Boyer 1994). The Levitus climatology is comprised of quality controlled ocean profile data averaged onto a global 1° latitude × 1° longitude grid at fixed standard depths.

3. Annual variability of the WHWP

In this section, we first describe seasonal variations of SST and subsurface temperature over the WHWP. Then, we show the surface heat flux of the WHWP. Finally, we examine tropospheric circulation patterns of the Walker and Hadley circulation cells associated with the WHWP.

a. SST and subsurface temperature

The seasonal variations of SST and of the subsurface topography of the 28.5°C isotherm are shown in Figs. 1 and 2, respectively. Figure 3 shows the annual march of average 28.5°C depth and mixed layer depth (MLD) over the WHWP, illustrating that the 28.5°C boundary is also an excellent proxy for the WHWP MLD. This correspondence holds for the ENP and IAS subregions as well (not shown). As an annual average both the 28.5°C isotherm and the WHWP mixed layer have a depth of about 25 m. As shown in Figs. 1a and 1b, the warm pool starts to develop in the ENP during the boreal early spring. By April and May, a dipole comprised of deep and shallow topography is arrayed along the 10°N parallel (Figs. 2b and 2c). The zonal dipole straddles the axis of strong northerly winds that emanate from the Gulf of Mexico over the Gulf of Tehuantepec during the late winter months (McCreary et al. 1989). Anticyclonic and cyclonic wind stress curls are correspondingly to the west and east of the northerly jet axis, respectively. This wind pattern, associated with negative and positive Ekman pumping, favors a deep mixed layer to the west and opposite to the east. This is manifested in the 28.5°C topography with the

onset of spring surface heating. By May, the WHWP is well developed in the ENP, but begins to shrink shoreward and spread along the coast where tropical storms frequently develop in the early summer. This becomes the core region of warm waters, which, in conjunction with increased activity of the intertropical convergence zone (ITCZ), trigger the onset of the Mexican and North American summer monsoons.

June is a transition period when the warm pool on the Atlantic side of Meso-America starts to develop, while the warm pool in the ENP decays. By July, water warmer than 28.5°C is well developed in the Gulf of Mexico and the WHWP covers the Gulf of Mexico and to less extent the ENP. In August, the warm water in the Gulf of Mexico reaches its maximum with a large area covered by water warmer than 29.5°C. By September, the warm pool has expanded south into the Caribbean and eastward into the western TNA, while the water in the Gulf of Mexico has cooled. Maximum warm pool development is attained in September with a large region of 28.5°C depths in excess of 40 m that ranges from the mid-Caribbean to the Atlantic seaward of the Bahamas islands. Significantly, this deep subregion corresponds to the most frequent tracks of developing late summer hurricanes that make landfall in North America. In particular, hurricane researchers frequently observe the rapid intensification of storms in the deep region south of Cuba when the tropospheric vertical wind shear is not unfavorable for development (Landsea, personal communication). By October, the warm pool still persists in the Caribbean and the western TNA, but the warm pool completely disappears from the Gulf of Mexico. The WHWP decays quickly after October (not shown).

b. Surface heat flux

Using the da Silva et al. data, WE01 showed that maximum of net heat flux in the WHWP region (7°N-27°N, 110°W-50°W) occurs around May which leads maximum SST in August-September by 3-4 months. This phase relationship suggests that the WHWP seasonal SST variations are induced primarily by surface net heat flux. We herein repeat the calculations of the WHWP seasonal SST, surface net heat flux, and heat storage tendency ($\rho C_P h \partial T / \partial t$) in WE01, by

using the NCEP-NCAR reanalysis, the NCEP SST, and the Levitus data. The Levitus data show that the mixed layer depth over the WHWP is on average about 25 m (Fig. 3), so we herein choose h=25 m in our calculation. The results are shown in Fig. 4. The phase relationships among the SST, net heat flux, and heat storage tendency are similar to those calculated from the da Silva et al. data set (see Fig. 2a of WE01). Maximum of the WHWP net heat flux in May leads maximum of the WHWP SST in September by 4 months, and the heat storage tendency is approximately in phase with the net heat flux. Although the phase relationship suggests that the surface net heat flux is a primary factor for the WHWP SST variations, other processes may not be ignored, especially during the boreal winter when surface cooling greatly exceeds the heat storage decrease.

The surface net heat flux is comprised of shortwave radiation, latent heat flux, longwave radiation, and sensible heat flux. The longwave radiation is defined as net longwave radiation across the sea surface, which is a function of air temperature, SST, cloudiness, and atmospheric vapor pressure. Thus, longwave radiation consists of two parts: (1) a cloud-free grey body flux from the sea surface and (2) a cloudiness factor that considers back-radiation to the ocean from the cloud ceiling. Figure 4b shows that the shortwave radiation, the latent heat flux, and the longwave radiation are the large terms, whereas the sensible heat flux has relatively small amplitude. The shortwave radiation is maximum in the spring, prior to the onset of summer and early fall cloudiness. The latent and sensible heat fluxes have their minimum values in the late spring and early summer owing to lower wind speeds associated with the seasonal south-north movement of the ITCZ. Minimum values of the longwave radiation occur in the boreal summer and early fall, associated with greater cloud cover and a corresponding increase in the downward longwave radiation from cloud ceilings. All of these, together, result in the maximum of net heat flux occurring in May.

c. Atmospheric circulation cells associated with the WHWP

In the last two sub-sections, we described and showed the development and formation of the WHWP. Warm water has a significant impact on organized tropical convection (e.g., Graham

and Barnett 1987) that is associated with atmospheric convergence/divergence and vertical motion. It is thus expected that the WHWP is associated with the adjacent Walker and Hadley circulation cells. We next examine the WHWP seasonal variations of tropospheric convergence/divergence and the associated Walker and Hadley cells.

To better show tropospheric circulation associated with the WHWP, we choose three levels of 200 hPa, 500 hPa, and 850 hPa as representative of the upper, middle, and lower troposphere, respectively. Figure 5 shows the boreal winter (January) climatologies of tropospheric circulation patterns. Centers of low (high) velocity potential are associated with divergent outflow (convergent inflow) winds. Figures 5a-c show that the center of upper tropospheric divergence and lower tropospheric convergence over central Brazil is characterized by middle tropospheric upward motion. This is consistent with the known boreal winter heat source over South America. The equatorial eastern Pacific, the equatorial eastern Atlantic, and the subtropical North Atlantic are associated with upper tropospheric convergence, lower tropospheric divergence, and middle tropospheric downward vertical motion (also see Mestas and Enfield 2001; Wang 2002a and b). Figure 5d shows the east-west circulation cell near the equator — the Atlantic zonal Walker cell. The air ascends over the equatorial region of northern South America, diverges eastward and westward aloft, and sinks in the equatorial eastern Atlantic and Pacific. Downward motion extends into the southeastern basins of both oceans. The meridional circulation between 80°W-40°W shows a deep-tropospheric Hadley cell (Fig. 5e). Air rises over South America, diverges northward at the upper troposphere, and descends in the subtropical North Atlantic. The equatorial zonal wind shows easterly wind in the lower troposphere and westerly wind in the upper troposphere, increasing northward into the subtropical North Atlantic (Fig. 5f). In addition to the low-level easterly flow over northern Brazil, the lower troposphere shows another low-level easterly flow over the Caribbean and western TNA near 12-15°N (Fig. 5f). The latter is manifestation of the Caribbean Low-Level Jet (CLLJ) described by Magana et al. (1999) and Mooers et al. (2001). The CLLJ is a key feature that covaries with the warm pool and other associated characteristics of the overlying troposphere (Knaff 1997).

The boreal summer (July) climatologies of tropospheric circulation are shown in Fig. 6. The centers of upper tropospheric divergence and lower tropospheric convergence associated with middle tropospheric ascent shift to the Northern Hemisphere (NH) and to the west, over the WHWP. Two subsiding limbs of the overturning are located over the subtropical western South Atlantic and eastern South Pacific. Consistent with these shifts, the Atlantic Walker circulation shows a weaker upward motion and a stronger downward motion (compared to the boreal winter) in the Amazon and equatorial eastern Atlantic, respectively. During the boreal summer, the Hadley circulation cell between 110°W-70°W shows that air rising around 10°N-15°N, diverging southward at the upper troposphere, descending in the subtropical South Atlantic, then crossing the equator at the surface and returning to the NH convergent region.

4. Interannual variability of the WHWP

As discussed in WE01, the WHWP also has significant interannual fluctuations of area and intensity. We next describe and examine the WHWP interannual variation and its associated atmospheric circulation cells.

a. WHWP indices

Two types of WHWP indices are calculated: intensity and area indices. The intensity index is the time series of SST anomalies for the rectangular region of 7°N-27°N, 110°W-50°W (WHWP SSTA). The area index is comprised of the anomalies of the area enclosed by the 28.5°C isotherm (WHWP area). We also calculate the intensity and area indices of the ENP and IAS separated by the Central American landmass. The oceanic factors important for the climate variability of the intertropical Americas include the Pacific El Niño, its projection into the tropical Atlantic (e.g., Enfield and Mayer 1997), the tropical Atlantic meridional SST gradient (e.g., Moura and Shukla 1981; Servain 1991; Chang et al. 1997; Xie 1999; Enfield et al. 1999), the equatorial Atlantic Niño (e.g., Zebiak 1993; Carton and Huang 1994; Latif and Grotzner 2000; Wang 2002b), and the interaction between the tropical Pacific and the tropical North Atlantic (Enfield and Alfaro 1999;

Giannini et al. 2000). Therefore, the WHWP SST anomalies may be compared statistically to a number of SST indices that are used to measure the above phenomena. The lagged correlation coefficients among various indices are listed in Tables 1 and 2.

Table 1 shows lagged correlations between various intensity indices. All of the indices in Table 1 are correlated above the 95% significant levels, except for the correlation between the ATL3 and ENP SST anomalies. From this table, several points can be mentioned. First, the WHWP SST anomalies are highly correlated with both the IAS and ENP SST anomalies at zero lag. Second, the anomalies of the ENP precede those of the IAS by 2 months, similar to the seasonal SST variations. Third, the interannual warming of the WHWP is influenced by both the Pacific El Niño and the TNA. The maximum correlation coefficients of the WHWP and TNA SST anomalies and of the WHWP and Nino3 SST anomalies are 0.68 and 0.63 with zero and three month lags, respectively. These statistics result from differing correlations between Nino3 SST and the ENP and IAS portions of the warm pool. Nino3 is more highly correlated with the ENP than the IAS, and nearly contemporaneous with the ENP SST anomalies. In contrast, the IAS lags Nino3 by six months and is more highly and contemporaneously correlated with the TNA. The former is expected from the proximity of the ENP to the equatorial eastern Pacific; the latter is consistent with a nearly contemporaneous relationship between the IAS and the TNA regions, and the fact that Nino3 precedes the TNA by 5-6 months (e.g., Enfield and Mayer 1997). The IAS SST anomalies are tightly connected with the TNA SST anomalies, suggesting that years with a warm (cool) TNA tend to be years when the warm pool is extensive (smaller) and the IAS is warm (cool). Clearly, the separation of the ENP and IAS regions by the isthmus land mass affects the relative influence of their respective ocean basins on their behavior. Fourth, the correlations of the warm pool with the tropical Atlantic meridional gradient mode (TNA-TSA) and the Atlantic Niño (ATL3) are relatively low (but significant) and they lag the warm pool SST anomalies. These suggest that the roles of the Atlantic meridional gradient mode and the equatorial Atlantic Niño in the warm pool are smaller than those of the Pacific El Niño and the TNA. The TSA does not significantly correlate with the WHWP indices (not shown), indicating that the TNA-TSA

correlation is acting mainly through its TNA component. Finally, the ENP SST anomalies are not significantly correlated with the ATL3 SST anomalies, as expected.

Table 2 shows the lagged correlation coefficients among the WHWP area (enclosed by 28.5°C) indices and their associated SST anomalies. All correlations between the whole and component indices are significant, indicating that the whole of the WHWP as seen by the atmosphere has significant contributions from both the Pacific and Atlantic sides of Central America. Since the WHWP area indices are highly correlated with the WHWP intensity indices, Table 2 does not include correlations with other climate phenomena as in Table 1. Again, the WHWP area anomalies are highly correlated with the IAS and ENP area anomalies and the ENP leads the IAS by 2 months. The WHWP area SST anomalies (i.e., SST anomalies over the area enclosed by the 28.5°C isotherm) are more highly correlated with the ENP area SST anomalies than with the IAS area SST anomalies**.**

The statistical correlations in Tables 1 and 2 cannot provide information about the amplitude of the WHWP indices. As an example, Fig. 7 shows the WHWP intensity and area anomalies, and the SST anomalies in the TNA region (6°N-22°N, 60°W-15°W) and in the Nino3 region (5°S-5°N, 150°W-90°W). The amplitude of the WHWP SST anomalies (Fig. 7a) is smaller than that for either the Nino3 or the TNA region. However, as in the western Pacific warm pool (e.g., Wang et al. 1999; Wang 2000), the WHWP anomalies occur at high SSTs where even small intensity changes, coupled with the large changes in area, can have a significant impact on the development of tropical convection and atmospheric circulation. In contrast, the area anomalies appear quite large taken as a percentage of a climatological warm pool month (July; see Fig.7b), in agreement with WE01.

During the 50-year period since 1950 there are five significant warm events in which the WHWP SST anomalies exceed 0.3°C for more than one month. The maximum WHWP SST anomalies for these warm events are centered in May 1958, May 1969, July 1983, October 1987, and July 1998 (Fig. 7a). All of these five warm events correspond to the prominent WHWP area (≥28.5°C) anomalies, as shown in Fig. 7b. Four of these warm events appear in the year after the

Pacific El Niño peak and they also coincide with strong warming of the TNA. The large warm pool in 1969 occurred in the middle of a moderate El Niño that began in 1968 and lasted through early 1970. Hence, it also occurred after El Niño conditions had been established during the preceding winter. However, the occurrence of El Niño is no guarantee of a large ensuing warm pool. Large warm pools fail to develop following four of the nine recognized El Niño events of the last 50 years.

Therefore, it appears that the warm pool is really responding to TNA warmings, which in turn frequently (but not invariably) occur in response to El Niño the winter before. These results are consistent with those that we see in the correlations: (1) the WHWP is highly correlated with TNA anomalies; (2) the TNA SST anomalies are correlated with, and lag by two seasons, the Pacific El Niño peaks. Hence, the Pacific El Niño and TNA work together to produce WHWP variations during the boreal summer following ENSO mature phases.

b. Atmospheric circulation cells

In order to investigate the Walker and Hadley circulation cells associated with the WHWP interannual warm events, we calculate the composites of SST and atmospheric circulation patterns. The composites are based on the five WHWP warm events of 1958, 1969, 1983, 1987, and 1998. Figure 8 shows the composites of July and September SST for these WHWP interannual warm events. As expected, Fig. 8a shows that the size of the WHWP for the interannual warm events during July is much larger than the July climatology (dark contour). Our calculations show that the area of the WHWP interannual warm events during July and September are larger by 96% and 27%, respectively for the five-event composites. The intensity of the WHWP interannual warm events during July and September increases by 0.40°C and 0.28°C, respectively. Landsea et al. (1999) showed that most of the Atlantic hurricanes occur during August-October, while Taylor et al. (2002) found that the early (May-July) Caribbean rainfall is more responsive to Atlantic SST anomalies than is the late summer (August-October) rainfall. Consistency of the WHWP SST variations with these studies will be discussed in Section 6b.

Pacific El Niño conditions were established during the winter seasons prior to the five largest warm pools and are key to understanding how large warm pools develop. In Fig. 9 we see composite-averaged maps of the velocity potential, divergent wind, and vertical velocity departures for the five winters (January of 1958, 1969, 1983, 1987, and 1998). Most prominent is a large convergent area over northern South America at 200 hPa and a corresponding outflow (divergence) at low-level (850 hPa). The upper convergence is fed by an anomalous northerly flow from the north, which in turn diverges from the Caribbean and subtropical North Atlantic. Comparison of these patterns to the climatology of Fig. 5 reveals a weakened Hadley circulation in the Atlantic sector, with less boreal winter convection over northern South America and weakened subsidence in the region of the North Atlantic subtropical high pressure system (Fig. 9d). The former is consistent with reduced rainfall observed over parts of Colombia, Venezuela, and northern Brazil (Ropelewski and Halpert 1987). The latter corresponds to a late winter weakening of the North Atlantic anticyclone and the associated northeast (NE) trade winds over its southern limb in the TNA region. With the weaker NE trades come reduced evaporation and entrainment (from below the oceanic mixed layer) during late winter and early spring, leading to warmer SST anomalies over the TNA region by late spring and early summer (Enfield and Mayer 1997 and others). The TNA warming along 5°-15°N (Enfield and Mayer 1997) extends well into the region of the Outer Antilles that by May sees SSTs above 27°C, required for large scale tropical convection at the start of the Caribbean rainy season. Thus, atmospheric circulation cells serve as a "tropospheric bridge" for transferring the Pacific El Niño SST anomalies to the Atlantic sector (also Wang 2002b and c) and inducing the TNA SST anomalies just at the time of year when the warm pool is developing.

Similar composite maps for July (1958, 1969, 1983, 1987, and 1998) illustrate the altered circulation associated with the large summer warm pools (Fig. 10). An upper tropospheric anomalous divergent outflow is centered near the ENP and extends over a wider region including the western Caribbean. This feature corresponds to the lower tropospheric anomalous convergent inflow (Figs. 10a and 10b). The equatorial zonal circulation shows anomalous ascending motion in the equatorial far eastern Pacific, and anomalous descending motion in the equatorial western

Atlantic (Fig. 10c). The anomalous Hadley circulation between 110°W-70°W shows ascent from the equator to 20°N, especially at the higher levels associated with deep convection. Consistent with the late-stage El Niño heating in the Pacific there is anomalous convergence and uplift over the ENP region, which is seen to reinforce the normal uplift near Central America. The strengthened outflow at 200 hPa feeds reinforced Hadley flows toward the subtropics of North America and the subtropical SE Pacific, with increased subsidence and surface outflow in the latter region. Once a large warm pool is formed, the atmosphere shows an altered circulation with the anomalous Hadley circulation ascending from the equator to 20°N (Fig. 10d).

5. The role of longwave radiation in WHWP SST anomalies

In the last section, both the correlation calculations and atmospheric circulation cells suggest that the Pacific ENSO variability is related to the WHWP variations. During winter preceding large warm pool there is a strong weakening of the Hadley cell, causing a spring ENSO teleconnection into the NE trades of the North Atlantic and a warming of TNA (e.g., Enfield and Mayer 1997). The TNA warming leads to an eastward expansion of the IAS portion of the warm pool through the additive effect of the adjacent warm anomalies near the windward islands. This warming of warm pool may be all that is needed to cause a large warm pool to persist through the summer. The question is that after the ENSO-related warming, what is process that maintains or amplifies SST anomaly growth in the region of warm pool?

A positive ocean-atmosphere feedback operating through latent heat flux has been hypothesized for the variations of TNA SST anomalies on interannual and longer time scales (e.g., Carton et al. 1996; Chang et al. 1997; Xie 1999). WE01 tested for a westward extension (in the WHWP) of this hypothesis by calculating the correlation between the WHWP SST and latent heat anomalies, using the da Silva et al. data set. They showed that the WHWP SST anomalies do not significantly correlate with the WHWP latent heat anomalies at any time lags, and suggested that the positive ocean-atmosphere feedback operating through latent heat flux is not a mechanism for the WHWP SST anomaly variations. However, they found a large correlation with a nearly

symmetrical distribution about zero lag between the WHWP surface longwave radiation and SST anomalies. Based on the da Silva data, they propose a positive ocean-atmosphere feedback operating through surface longwave radiation and associated cloudiness being responsible for the WHWP SST anomaly growth at the interannual time scale. Given an increase in SST anomalies, the atmosphere shows an anomalous increase in deep convective activity and atmospheric cloudiness. The increase in convection and cloudiness results in less longwave radiation loss from the sea surface, which then reinforces the original SST anomalies.

Using the alternate NCEP-NCAR reanalysis data and NCEP SST data, we herein repeat the calculations of WE01 as shown in Fig. 11, for confirmation of the WE01 results using the da Silva et al. data. The results are, in fact, similar to those of WE01 from the da Silva et al. data. Although the positive correlation between the WHWP SST and latent heat anomalies is increased in comparison with the da Silva et al. data, the WHWP latent heat anomalies still lag the WHWP SST anomalies by three months. Also, Fig. 11b shows that the maximum negative correlation between the WHWP shortwave radiation and SST anomalies occurs when the shortwave radiation anomalies lag the WHWP SST anomalies by two months. These phase lags imply that latent heat and shortwave radiation anomalies do not force SST anomalies in the WHWP region, rather they are a consequence of the SST anomalies. Warm SST anomalies increase convective cloudiness that reduces the solar radiation into the ocean (not shown). The decrease of shortwave radiation anomalies tends to damp/cool the original warm SST anomalies two months later (Fig. 11b). The lagged and positive correlation of Fig. 11a also suggests a damped effect of latent heat flux.

The cross-correlation between the longwave radiation and SST anomalies is again large and shows a nearly symmetrical distribution about zero lag (Fig. 11c). A negative correlation between the longwave radiation and cloud anomalies also occurs at zero lag (Fig. 11d). Since evaporation lags SST in the WHWP (Fig. 11a), a possible alternate source of increased cloudiness is through reduced vertical wind shear, which allows deep convection to develop (Knaff 1997). In order to further examine the distribution of longwave radiation anomalies in the WHWP and the relationship between the WHWP SST and longwave radiation anomalies, Figs. 12 and 13 show

the composite of longwave radiation anomalies in July for the WHWP warm events and the time series of the WHWP SST and longwave radiation anomalies, respectively. The WHWP interannual warm events correspond to negative longwave radiation anomalies in the WHWP region (Fig. 12). Figure 13 clearly shows an out-of-phase relationship between the SST and longwave radiation anomalies. The cloudiness anomalies also display a similar spatial distribution to Fig. 12 and an out-of-phase relation with longwave radiation anomalies (not shown).

Figures 11-13 are consistent with the hypothesis of a positive feedback between the longwave radiation and SST anomalies associated with cloudiness variations. Positive SST anomalies are associated with negative SLP anomalies (Fig. 11e). The positive SST anomalies cause an anomalous increase in deep convective activity and atmospheric cloudiness (Fig. 11f). The increase in convection and cloudiness results in less longwave radiation loss from the sea surface, which then reinforces the original SST anomalies (Figs. 11c, 11d, 12, and 13). Therefore, the longwave radiation feedback process can amplify the SST anomalies of warm pool that may be initiated by the Pacific ENSO.

We also perform similar correlation calculations for the IAS and ENP components of warm pool (not shown). The results for the IAS are similar to the WHWP in Fig. 11. However, the ENP behaves differently. The maximum correlation of –0.23 (below the 95% significant level) between the ENP longwave radiation and SST anomalies occurs when the ENP longwave radiation anomalies lag the ENP SST anomalies by 2 months. The ENP SLP anomalies do not significantly correlate with the ENP cloud anomalies. All of these suggest that the positive ocean-atmosphere feedback operating through longwave radiation and associated cloudiness is not responsible for the ENP warmings on interannual scale. The ENP probably warms due to a direct oceanic connection to the equator, such as advection. The Atlantic warming appears to be the result of tropospheric changes initiated by the Pacific ENSO. These changes most likely involve a reduction in static stability that favors increased cloudiness at the same time that decreased easterlies cause an initial warming to take place. Knaff (1997) discusses the tropospheric changes that accompany IAS warming. Those that affect convection include static stability, vertical shear and the intensity of the

tropical upper troposphere trough (TUTT). The increased cloudiness reinforces the warming which in turn feeds back on the tropospheric instability. Because the Hadley cell mechanism of this tropospheric bridge operates mainly in the Atlantic sector, the ENP is mostly unaffected by this process.

6. Discussion and summary

The eastward expansion and westward contraction of the Eastern Hemisphere warm pool in the western Pacific, associated with large changes in atmospheric convection, plays an important role in the evolution of ENSO (e.g., Philander 1990; Neelin et al. 1998). The shift of this warm pool and convective activity leads to altered Walker and Hadley circulations (e.g., Oort and Yienger 1996; Wang and Weisberg 1998; Wang 2002a) and then affects climate variations on a global scale. The WHWP is the second-largest tropical warm pool on Earth. The WHWP also has a large annual cycle and the interannual fluctuations of its area are comparable to the annual mean, although it does not undergo large anomalous zonal excursions such as occur in the western Pacific. The annual development and demise of the WHWP are associated with marked seasonal changes in tropospheric heat, moisture and stability over the inter-tropical Americas, resulting in contrasting wet and dry seasons and the annual development of tropical storms and hurricanes on both sides of Central America.

a. A tropospheric bridge for the tropical Atlantic

The climatology of the NCEP/NCAR reanalysis field reveals that the WHWP alternates with northern South America as the seasonal source of Walker and Hadley circulations in the Western Hemisphere (Figs. 5 and 6). During a normal boreal winter, the centers of upper tropospheric divergence and lower tropospheric convergence, and middle tropospheric upward motion are over South America with a Hadley cell subsiding primarily over the subtropical North Atlantic north of 20°N (Fig. 5). That subsidence helps sustain a strong North Atlantic anticyclone and associated NE trade winds over its southern limb in the TNA (5-15°N). As the WHWP

develops and forms in the late boreal spring, the centers of upper tropospheric divergence and lower tropospheric convergence associated with middle tropospheric ascent shift to the WHWP region. Once established, the summer Hadley circulation emanates from a single ascent region over the WHWP, around 10°N-15°N, and forks out to two subsidence regions in the subtropical South Atlantic and South Pacific.

Consideration of the five largest warm pool occurrences (1950-1999) shows that they all occurred in the summers following boreal winter El Niño developments (1958, 1969, 1983, 1987, and 1998). The composited maps reveal how the El Niño SST anomalies are transferred to the Atlantic sector via the tropospheric bridge (also see Wang 2002b and c) and how the induced North Atlantic SST anomalies precede the subsequent anomalous warm pool growth. As the El Niño warming culminates near the end of the calendar year, an alteration of the low-latitude direct circulation occurs, featuring (1) an anomalous weakening of the convection over northern South America, (2) Walker circulation anomalies along the equatorial strip to the east and west, and (3) a weakened northward Hadley flow aloft. The Hadley weakening results in less subsidence over the subtropical North Atlantic, an associated breakdown of the anticyclone and a weakening of the NE trades in the TNA. The wind weakening leads to less evaporative surface cooling and entrainment of colder water from below the shallow mixed layer (Enfield and Mayer 1997 and others). The opposite is presumed to occur during boreal winters with unusually cool SST in the equatorial Pacific.

The above mechanism is observed to work most efficiently during the early months of the calendar year following large ENSO anomalies in the Pacific, and results in maximum positive SST anomalies in the TNA during the late boreal spring and early summer when the WHWP is developing and SSTs over 27°C, required for the development of large scale tropical convection, extend eastward into the western portion of the TNA. The TNA anomalies thus expand the WHWP area and increase the WHWP SST anomalies, just when warm pool development is taking place. Our analysis of surface flux terms (Section 5) suggests that the positive feedback process involving longwave radiation and cloudiness then sets in over the IAS and leads to extended and

amplified warm pool anomalies during the early WHWP season (MJJ), with some carryover to the late season (ASO). This also seems to explain why the composite anomalies for the five warm events are comparatively larger during July (96%) than September (27%).

The deep Hadley circulation cell suggests that the WHWP may also relate to interannual climate variability in the Southern Hemisphere, especially in respect of Pacific ENSO connectivity. Thus, as the Atlantic warms in the boreal spring following the Pacific El Niño peak, the warm pool expands and warms more than usual, aided by the longwave radiation feedback. Simultaneously, the boreal summer Hadley circulation accelerates into the tropical South Pacific. It is not hard to surmise that the increased subsidence off Peru strengthens the subtropical anticyclone there and hastens the switch back to cool or La Niña type conditions near mid-year.

b. Thermodynamics of the warm pool

The seasonal and interannual variability of the WHWP is examined by analyzing the NCEP-NCAR reanalysis field and the NCEP SST from 1950-1999, and the Levitus climatological subsurface temperature. The results are consistent with those of WE01 concluding from the da Silva et al. (1994) data from 1945-1993. The WHWP shows a large seasonal cycle and significant interannual time scale variations. Seasonally, the surface net heat flux seems to be primarily responsible for the WHWP warming, although the roles of advection and entrainment in the warm pool seem to be important (especially in winter) and deserve further attention. Although the WHWP SST anomalies are not large compared to the annual cycle or to the Pacific El Niño or to the TNA SST anomalies, the WHWP variability occurs at high temperatures where small changes can induce large effects on tropical convection. Moreover, the changes in SST anomalies are highly correlated with large expansions and contractions in the boreal summer area covered by SSTs over 28.5°C.

All of the data sets of the da Silva et al. data, the NCEP-NCAR reanalysis field, and the NCEP SST show that the positive ocean-atmosphere feedback operating through latent heat flux, hypothesized for the variations of TNA SST anomalies (Carton et al. 1996; Chang et al. 1997; Xie

1999), is not a mechanism for the WHWP SST anomaly variations on interannual time scale. These data suggest that a positive ocean-atmosphere feedback operating through surface longwave radiation and associated cloudiness may explain the growth and persistence of WHWP anomalies. Given an increase in SST anomalies, the atmosphere shows an anomalous increase in deep convective activity and atmospheric cloudiness. The increase in convection and cloudiness results in less longwave radiation loss, which then reinforces the original SST anomalies. We have to keep in mind that the positive longwave feedback process is inferred from statistical analysis of observed data only. Given that the statistical approach is not perfect for inferring information about ocean-atmosphere interactions, this feedback process needs to be further studied, especially through coupled ocean-atmosphere models for its validation in the WHWP.

The longwave radiation feedback in the WHWP is consistent with previous research. It has been shown that the IAS radiates more (less) energy to space during periods of high (low) SLP (Knaff 1997), a fact that is consistent with the inverse relationship between SST and SLP (Fig. 11e) and with the relationships among longwave radiation, SST, and cloud (Figs. 11c, 11d, 12, and 13). This feedback is also consistent with the results of Ramanathan and Collins (1991) who observed a positive feedback between SST and cloud longwave forcing during the Pacific 1986-87 El Niño. They also argued that the positive feedbacks due to the clouds and greenhouse gases in the atmosphere are diminished by the significant decrease in cloud shortwave forcing. Philander et al. (1996) proposed a positive ocean-atmosphere feedback operating through shortwave radiation due to low-level stratus clouds over the cold water region of the southeast tropical Pacific. In their feedback, cold SSTs strengthen the atmospheric inversion and hence produce more low-level stratus clouds, which decrease the temperature further by reducing shortwave radiation. However, the WHWP is associated with warm water which produces high-level and convective clouds. These environmental differences seem to favor the clouds participating through longwave radiation in the WHWP region rather than through shortwave radiation.

Geographically, the WHWP is separated into the ENP and the IAS by the narrow Meso-American landmass. Although the atmosphere responds to the WHWP as a monolithic whole, the

ENP and the IAS seem to have distinct ocean thermodynamics. The IAS SST variations behave more like those of the WHWP as a whole than the ENP. The surface net heat flux is not primarily responsible for the seasonal SST variation in the ENP. The positive ocean-atmosphere feedback operating through surface longwave radiation and associated cloudiness is not a mechanism for the ENP SST anomalies. Since the ENP warm pool spans the ITCZ, the seasonal SST in the ENP may be related to the seasonal movement of the ITCZ. Interannually, however, the ENP intensity and size anomalies are probably controlled directly by the anomalous Pacific mixed layer associated with extreme ENSO phases.

The Pacific ENSO variability is also related to the WHWP variations as a whole, and those of the IAS, but less strongly and with large lags. The correlation lags strongly suggest that the Pacific ENSO influence enters the WHWP and IAS by proxy, i.e., via the tropospheric bridge to the TNA (Enfield and Mayer 1997). As the TNA warms in the boreal spring following the Pacific El Niño peak, this leads to an eastward expansion of the IAS portion of the warm pool through the additive effect of the adjacent warm anomalies near the windward islands. This ENSO-related warming may be further amplified by the positive longwave feedback process that leads to a large warm pool. This also explains why the Pacific ENSO-related warm pool maxima typically come in the boreal summer following the Pacific ENSO peak, i.e., when the Pacific El Niño is in decline or has succumbed to La Niña. However, a further study is needed to understand why warm pool growth occurs following some El Niño peaks and but not others.

The warm pool variability has significant effects locally in the IAS region, as well as remotely. As the warm pool develops and the IAS rainy season begins (around May), warmer SSTs are associated with a warmer and moister troposphere, reduced SLP, weaker easterly trade winds, less vertical wind shear and weakened subsidence aloft (Gray 1968 and 1979; Knaff 1997). The summer maximum of the WHWP area index is therefore consistent with the factors that favor a contemporaneous, strong rainy season and a higher frequency and greater intensity of tropical cyclones (Knaff 1997; Neumann 1993; Landsea 1993; Chen and Taylor 2002). These factors also operate interannually in the same way (Knaff 1997). Years with a well-developed

warm pool have lower SLP and vertical shear, greater moist instability over the WHWP, and a weakened tropical upper tropospheric trough (TUTT). These conditions lead to generally greater summer rainfall over the IAS and Central America (Enfield 1996; Enfield and Alfaro 1999; Giannini et al. 2000) and an increase in tropical cyclone activity (Knaff 1997).

In this study we have found that El Niño leads to a large and intense warm pool by proxy through the TNA. Taylor et al. (2002) have recently shown a similar result for Caribbean rainy season. The boreal summer rainy season is not temporally uniform in its development and interannual dependencies and the early and late season should properly be considered separately. The TNA influence on Caribbean rainfall prevails in the early season when the warm pool is expanding and changes in the size and intensity of the WHWP can have a conditioning effect on the overlying troposphere. Conversely, in the late season the entire IAS and TNA are covered by water warm enough to support large scale, organized convection, such that superimposed anomalies have less additional effect. This is also consistent with our finding that the direct circulation anomalies emanating from a changed warm pool in July are larger than those in September of the same years (Fig. 8).

Finally, although the independent data sets show a consistent result regarding the WHWP seasonal and interannual variability, more studies of the WHWP are needed. In particular, numerical models are needed to investigate the WHWP seasonal SST variations and the positive ocean-atmosphere feedback operating through longwave radiation and associated cloudiness being responsible for amplification or persistence of the WHWP SST anomalies. We need to understand why a large warm pool occurs following some El Niño events, but not others. A better understanding of WHWP SST variations may lead to improved forecasts of hurricanes in the eastern Pacific and Atlantic, and rainfall from northern South America through Central America to the southern tier of the United States.

Acknowledgment. This work was supported by a grant from NOAA Office of Global Programs through CLIVAR-Pacific Program, by NOAA Environmental Research Laboratories

through their base funding of Atlantic Oceanographic and Meteorological Laboratory (AOML), and by National Natural Science Foundation of China through Grant 40176003.

References

Carton, J. A., and B. Huang, 1994: Warm events in the tropical Atlantic. *J. Phys. Oceanogr*., **24**, 888-903.

Carton, J. A., X. Cao, B. Giese, and A. M. Da Silva, 1996: Decadal and interannual SST variability in the tropical Atlantic Ocean. *J. Phys. Oceanogr*., **26**, 1165-1175.

Chang, P., L. Ji, and H. Li, 1997: A decadal climate variation in the tropical Atlantic Ocean from thermodynamic air-sea interactions. *Nature*, **385**, 516-518.

Chen, A. A., and M. A. Taylor, 2002: Investigating the link between early season Caribbean rainfall and the El Niño+1 year. *Int. J. Climatol*., **22**, 87-106.

da Silva, A. M., C. C.Young, and S. Levitus, 1994: Atlas of surface marine data 1994. Vol. 1. Algorithms and procedures, NOAA Atlas NESDIS 6, US Dept. of Commence, Washington, DC, 83 pp.

Enfield, D.B., 1996: Relationships of inter-American rainfall to tropical Atlantic and Pacific SST variability. *Geophys. Res. Lett*., **23**, 3505-3508.

Enfield, D. B., and D. A. Mayer, 1997: Tropical Atlantic sea surface temperature variability and its relation to El Niño-Southern Oscillation. *J. Geophys. Res*., **102**, 929-945.

Enfield, D.B., and E.J. Alfaro, 1999: The dependence of Caribbean rainfall on the interaction of the tropical Atlantic and Pacific Oceans. *J. Climate*, **12**, 2093-2103.

Enfield, D. B., A. M. Mestas-Nunez, D. A. Mayer, and L. Cid-Serrano, 1999: How ubiquitous is the dipole relationship in tropical Atlantic sea surface temperature? *J. Geophys. Res*., **104**, 7841-7848.

Giannini, A., Y. Kushnir, and M. A. Cane, 2000: Interannual variability of Caribbean rainfall, ENSO and the Atlantic Ocean. *J. Climate*, **13**, 297–311.

Graham, N. E., and T. P. Barnett, 1987: Sea surface temperature, surface wind divergence, and convection over tropical oceans. *Science*, **238**, 657-659.

Gray, W. M., 1968: Global view of the origions of tropical disturbances and storms. *Mon. Wea. Rev*., **96**, 669-700.

Gray, W. M., 1979: Hurricanes: Their formation, structure, and likely role in the tropical circulation. Meteorology Over the Tropical Oceans, D. B. Shaw, Ed., Roy. Meteor. Soc., 155-218.

Kalnay, E., and Co-authors, 1996: The NCEP/NCAR 40-year reanalysis project. *Bull. Am. Meteorol. Soc*., **77**, 437-471.

Knaff, J. A., 1997: Implications of summertime sea level pressure anomalies in the tropical Atlantic region. *J. Climate*, **10**, 789-804.

Krishnamurti, T. N., 1971: Tropical east-west circulations during the northern summer. *J. Atmos. Sci*., **28**, 1342-1347.

Krishnamurti, T. N., M. Kanamitsu, W. J. Koss, and J. D. Lee, 1973: Tropical east-west circulations during the Northern Winter. *J. Atmos. Sci.*, **30**, 780-787.

Landsea, C. W., 1993: A climatology of intense (or major) Atlantic hurricanes. *Mon. Wea. Rev.*, **121**, 1703-1713.

Landsea, C. W., R. A. Pielke, A. M. Mestas-Nunez, and J. A. Knaff, 1999: Atlantic basin hurricanes: Indices of climatic changes. *Climatic Change*, **42**, 89-129.

Latif, M., and A. Grotzner, 2000: The equatorial Atlantic oscillation and its response to ENSO. *Clim. Dyn*., **16**, 213-218.

Levitus, S., and T. P. Boyer, 1994: *World Ocean Atlas*. Vol. 4, *Temperature.* NOAA Atlas NESDIS 4, U.S. Government Printing Office, Washington, DC, 117pp.

Magaña, V., J. A. Amador, and S. Medina, 1999: The midsummer drought over Mexico and central America. *J. Climate*, **12**, 1577-1588.

Mancuso, R. L., 1967: A numerical procedure for computing fields of streamfunction and velocity potential. *J. Appl. Meteorol*., **6**, 994-1001.

McCreary, J. P., H. S. Lee, and D. B. Enfield, 1989: The response of the coastal ocean to strong

offshore winds: With application to circulations in the Gulfs of Tehuantepec and Papagayo. *J. Mar. Res*., **47**, 81-109.

Mestas-Nunez, A. M., and D. B. Enfield, 2001: Eastern equatorial Pacific SST variability: ENSO and non-ENSO components and their climatic associations. *J. Climate*, **14**, 391-402.

Mooers, C., and Co-authors, 2001: IAI/CRN-73: R/V Justo Sierra Cruise Report. University of Miami, 15 pp. [Available from RSMAS/UM, 4600 Rickenbacker Causeway, Miami, FL 33149.]

Moura, A., and J. Shukla, 1981: On the dynamics of droughts in northeast Brazil: observations, theory, and numerical experiments with a general circulation model. *J. Atmos. Sc*i., **38**, 2653-2675.

Neelin, J. D/, D. S. Battisti, A. C. Hirst, F.-F. Jin, Y. Wakata, T. Yamagata, S. E. Zebiak, 1998: ENSO theory. *J. Geophys. Res*., **103**, 14262-14290.

Neumann, C. J., Global overview, 1993: Global Guide to Tropical Cyclone Forecasting. WMO/TC No. 560, Report No. TCP-31, World Meteorological Organization, Geneva, pp.1.1-1.43.

Oort, A. H., and J. J. Yienger, 1996: Observed interannual variability in the Hadley Circulation and its connection to ENSO. *J. Climate*, **9**, 2751-2767.

Philander, S. G., 1990: El Niño, La Niña, and the Southern Oscillation. Academic Press, London, 289pp.

Philander, S. G. H., D. Gu, D. Halpern, G. Lambert, N. C. Lau, and R. C. Pacanowski, 1996: Why the ITCZ is mostly north of the equator. *J. Climate*, **9**, 2958-2972.

Ramanathan, V., and W. Collins, 1991: Thermodynamic regulation of ocean warming by cirrus clouds deduced from observations of the 1987 El Niño. *Nature*, **351**, 27-32.

Ropelewski, C. F., and M. S. Halpert, 1987: Global and regional scale precipitation patterns associated with the El Niño/Southern Oscillation. *Mon. Wea. Rev*., **115**, 1606-1626.

Sciremammano, F., 1979: A suggestion for the presentation of correlations and their significance levels. *J. Phys. Oceanogr*, **9**, 1273-1276.

Servain, J., 1991: Simple climatic indices for the tropical Atlantic Ocean and some applications. *J. Geophys. Res.*, **96**, 15,137-15,146.

Smith, T. M., R. W. Reynolds, R. E. Livezey, and D. C. Stokes, 1996: Reconstruction of historical sea surface temperature using empirical orthogonal functions. *J. Climate*, **9**, 1403-1420.

Taylor, M. A., D. B. Enfield, and A. A. Chen, 2002: The influence of the tropical Atlantic vs. the tropical Pacific on Caribbean Rainfall. *J. Geophys. Res.*, **107**, 10.1029/2001JC001097.

Wang, C., and R. H. Weisberg, 1998: Climate variability of the coupled tropical-extratropical ocean-atmosphere system. *Geophys. Res. Lett.*, **25**, 3979-3982.

Wang, C., R. H. Weisberg, and J. I. Virmani, 1999: Western Pacific interannual variability associated with the El Niño-Southern Oscillation. *J. Geophys. Res.*, **104**, 5131-5149.

Wang, C., 2000: On the atmospheric responses to tropical Pacific heating during the mature phase of El Niño. *J. Atmos. Sci.*, **57**, 3767-3781.

Wang, C., and D. B. Enfield, 2001: The tropical Western Hemisphere warm pool. *Geophys. Res. Lett.*, **28**, 1635-1638.

Wang, C., 2002a: Atmospheric circulation cells associated with the El Niño-Southern Oscillation. *J. Climate*, **15**, 399-419.

Wang, C., 2002b: Atlantic climate variability and its associated atmospheric circulation cells. *J. Climate*, **15**, 1516-1536.

Wang, C., 2002c: ENSO and atmospheric circulation cells. *CLIVAR Exchanges*, **7**, 9-11.

Webster, P. J., and R. Lukas, 1992: The Tropical Ocean/Global Atmosphere Coupled Ocean-atmosphere Response Experiment (COARE). *Bull. Amer. Meteor. Soc.*, **73**, 1377-1416.

Xie, S. P.,1999: A dynamic ocean-atmosphere model of the tropical Atlantic decadal variability. *J. Climate*, **12**, 64-70.

Zebiak, S. E., 1993: Air-sea interaction in the equatorial Atlantic region. *J. Climate*, **6**, 1567-1586.

Figure Captions

Figure 1. Seasonal distributions of SST for the tropical WHWP: (a) March, (b) April, (c) May, (d) June, (e) July, (f) August, (g) September, and (h) October. The shading and dark contour represent water warmer than 28.5°C. The data are from the NCEP SST.

Figure 2. Seasonal distributions of depth (m) of 28.5°C isotherm: (a) March, (b) April, (c) May, (d) June, (e) July, (f) August, (g) September, and (h) October. The data are from the Levitus climatological subsurface temperature.

Figure 3. Seasonal variations of average 28.5°C depth (solid line) and mixed layer depth (MLD) (dashed line) over the WHWP. The data are from the Levitus climatological data.

Figure 4. (a) Seasonal variations of SST, surface net heat flux (shortwave radiation minus latent heat flux, longwave radiation, and sensible heat flux), and heat storage (HS) tendency ($\rho C_P h \partial T / \partial t$) in the WHWP region (7°N-27°N, 110°W-50°W). (b) Seasonal variations of shortwave radiation, latent heat flux, longwave radiation, and sensible heat flux in the WHWP region.

Figure 5. The boreal winter (January) climatologies of tropospheric circulation patterns. (a) 200 hPa velocity potential (10^6 m^2/s) and divergent wind (m/s), (b) 850 hPa velocity potential (10^6 m^2/s) and divergent wind (m/s), (c) 500 hPa vertical velocity (10^{-4} hPa/s), (d) zonal-vertical (in unit of hPa) circulation by averaging divergent wind and vertical velocity between 2.5°S-2.5°N, (e) meridional-vertical circulation by averaging divergent wind and vertical velocity between 80°W-40°W, (f) the total zonal wind between 80°W-40°W. The vertical velocity is taken the negative of the pressure vertical velocity in the reanalysis, i.e., positive values indicate an upward movement of air parcels. Positive values are shaded.

Figure 6. The boreal summer (July) climatologies of tropospheric circulation patterns. (a) 200 hPa velocity potential (10^6 m^2/s) and divergent wind (m/s), (b) 850 hPa velocity potential (10^6 m^2/s) and divergent wind (m/s), (c) 500 hPa vertical velocity (10^{-4} hPa/s), (d) zonal-vertical (in unit of hPa) circulation by averaging divergent wind and vertical velocity between 2.5°S-2.5°N, (e) meridional-vertical circulation by averaging divergent wind and vertical velocity between 110°W-70°W, (f) the total zonal wind between 110°W-70°W. The vertical velocity is taken the negative of the pressure vertical velocity in the reanalysis, i.e., positive values indicate an upward movement of air parcels. Positive values are shaded.

Figure 7. Three-month running means of (a) SST anomalies in the WHWP region (7°N-27°N, 110°W-50°W), (b) WHWP area anomalies (%) for SST warmer than 28.5°C, (c) SST anomalies in the TNA region (6°N-22°N, 60°W-15°W); and (d) SST anomalies in the Nino3 region (5°S-5°N, 150°W-90°W). The WHWP area anomalies (in unit of percentage) are calculated as anomalies of area (≥ 28.5°C) divided by the July climatological warm pool area. The largest warm pool area anomalies are a large fraction of the mean WHWP area.

Figure 8. SST composites in (a) July and (b) September for the WHWP interannual warm events. The composites are calculated by averaging over the warm years of 1958, 1969, 1983, 1987, and 1998. The shading represents water warmer than 28.5°C. The dark contour is climatological SST warmer than 28.5°C.

Figure 9. Anomalous composites for the WHWP interannual warm events (January). (a) 200 hPa velocity potential anomalies (10^6 m^2/s) and divergent wind anomalies (m/s), (b) 850 hPa velocity potential anomalies (10^6 m^2/s) and divergent wind anomalies (m/s), (c) zonal-vertical (in unit of hPa) circulation by averaging divergent wind anomalies and vertical velocity anomalies between 2.5°S-2.5°N, and (d) meridional-vertical circulation by averaging divergent wind anomalies and

vertical velocity anomalies between 80°W-40°W. The composites are calculated by averaging January anomaly values of 1958, 1969, 1983, 1987, and 1998.

Figure 10. Anomalous composites for the WHWP interannual warm events (July). (a) 200 hPa velocity potential anomalies (10^6 m^2/s) and divergent wind anomalies (m/s), (b) 850 hPa velocity potential anomalies (10^6 m^2/s) and divergent wind anomalies (m/s), (c) zonal-vertical (in unit of hPa) circulation by averaging divergent wind anomalies and vertical velocity anomalies between 2.5°S-2.5°N, and (d) meridional-vertical circulation by averaging divergent wind anomalies and vertical velocity anomalies between 110°W-70°W. The composites are calculated by averaging July anomaly values of 1958, 1969, 1983, 1987, and 1998.

Figure 11. The lagged cross-correlation coefficients between (a) the WHWP latent heat flux and SST anomalies, (b) the WHWP shortwave radiation and SST anomalies, (c) the WHWP longwave radiation and SST anomalies, (d) the WHWP longwave radiation and cloud cover anomalies, (e) the WHWP SLP and SST anomalies, and (f) the WHWP SLP and cloud cover anomalies. The horizontal dashed lines represent 95% significance level. Degrees of freedom are determined by the integral time scale after Sciremammano (1979). Negative lags imply that the second variable leads the first. Shortwave radiation is positive into the ocean; others (longwave radiation, latent heat flux, and sensible heat flux) are positive out of the ocean.

Figure 12. Composite of longwave radiation anomalies (W m^{-2}) for the WHWP interannual warm events. The composite is calculated by averaging July longwave radiation anomalies over the warm years of 1958, 1969, 1983, 1987, and 1998. The shading represents longwave radiation anomalies less than –2.0 W m^{-2}.

Figure 13. Three-month running means of SST anomalies (solid line) and longwave radiation anomalies (dashed line) in the WHWP region (7°N-27°N, 110°W-50°W). Anomalies are normalized by standard deviations.

Table Captions

Table 1. Lagged correlations between various intensity indices. WHWP SSTA is SST anomalies in the region of 7°N-27°N, 110°W-50°W. IAS and ENP SSTA are SST anomalies of the WHWP separated by the Central-America landmass. Nino3 SSTA is SST anomalies in the region of 5°S-5°N, 150°W-90°W. TNA SSTA is SST anomalies in the region of 6°N-22°N, 60°W-15°W. TNA-TSA is SST anomaly difference between the TNA and TSA (0°-20°S, 30°W-10°E). ATL3 SSTA is SST anomalies in the region of 3°S-3°N, 20°W-0°. Positive (negative) numbers in parentheses are months by which row indices are leading (lagging) column indices. All of these correlation coefficients are significant at 95%, except for the correlation between ATL3 and ENP SSTA (denoted by *).

Table 2. Lagged correlations between various area indices. The indices are defined by anomalies of area enclosed by the 28.5°C isotherm and SST anomalies over the area enclosed by the 28.5°C isotherm. Positive (negative) numbers in parentheses are months by which row indices are leading (lagging) column indices. All of these correlation coefficients are significant at 95%.

Table 1. Lagged correlations between various intensity indices. WHWP SSTA is SST anomalies in the region of 7°N-27°N, 110°W-50°W. IAS and ENP SSTA are SST anomalies of the WHWP separated by the Central-America landmass. Nino3 SSTA is SST anomalies in the region of 5°S-5°N, 150°W-90°W. TNA SSTA is SST anomalies in the region of 6°N-22°N, 60°W-15°W. TNA-TSA is SST anomaly difference between the TNA and TSA (0°-20°S, 30°W-10°E). ATL3 SSTA is SST anomalies in the region of 3°S-3°N, 20°W-0°. Positive (negative) numbers in parentheses are months by which row indices are leading (lagging) column indices. All of these correlation coefficients are significant at 95%, except for the correlation between ATL3 and ENP SSTA (denoted by *).

	WHWP SSTA	IAS SSTA	ENP SSTA
IAS SSTA	0.93 (0)		
ENP SSTA	0.82 (0)	0.58 (+2)	
Nino3 SSTA	0.63 (+3)	0.49 (+6)	0.81 (+1)
TNA SSTA	0.68 (0)	0.70 (+1)	0.51 (-1)
TNA-TSA	0.38 (-2)	0.40 (-1)	0.30 (-7)
ATL3 SSTA	0.27 (-7)	0.26 (-7)	0.21 (-7)*

Table 2. Lagged correlations between various area indices. The indices are defined by anomalies of area enclosed by the 28.5°C isotherm and SST anomalies over the area enclosed by the 28.5°C isotherm. Positive (negative) numbers in parentheses are months by which row indices are leading (lagging) column indices. All of these correlation coefficients are significant at 95%.

	WHWP Area	IAS Area	ENP Area	WHWP Area SSTA	IAS Area SSTA
IAS Area	0.85 (0)				
ENP Area	0.80 (+1)	0.44 (+2)			
WHWP Area SSTA	0.64 (+1)	0.37 (+3)	0.73 (+1)		
IAS Area SSTA	0.65 (0)	0.68 (0)	0.39 (-1)	0.39 (0)	
ENP Area SSTA	0.58 (+2)	0.36 (+4)	0.72 (+1)	0.92 (0)	0.27 (+2)

Western Hemisphere Warm Pool (WHWP)

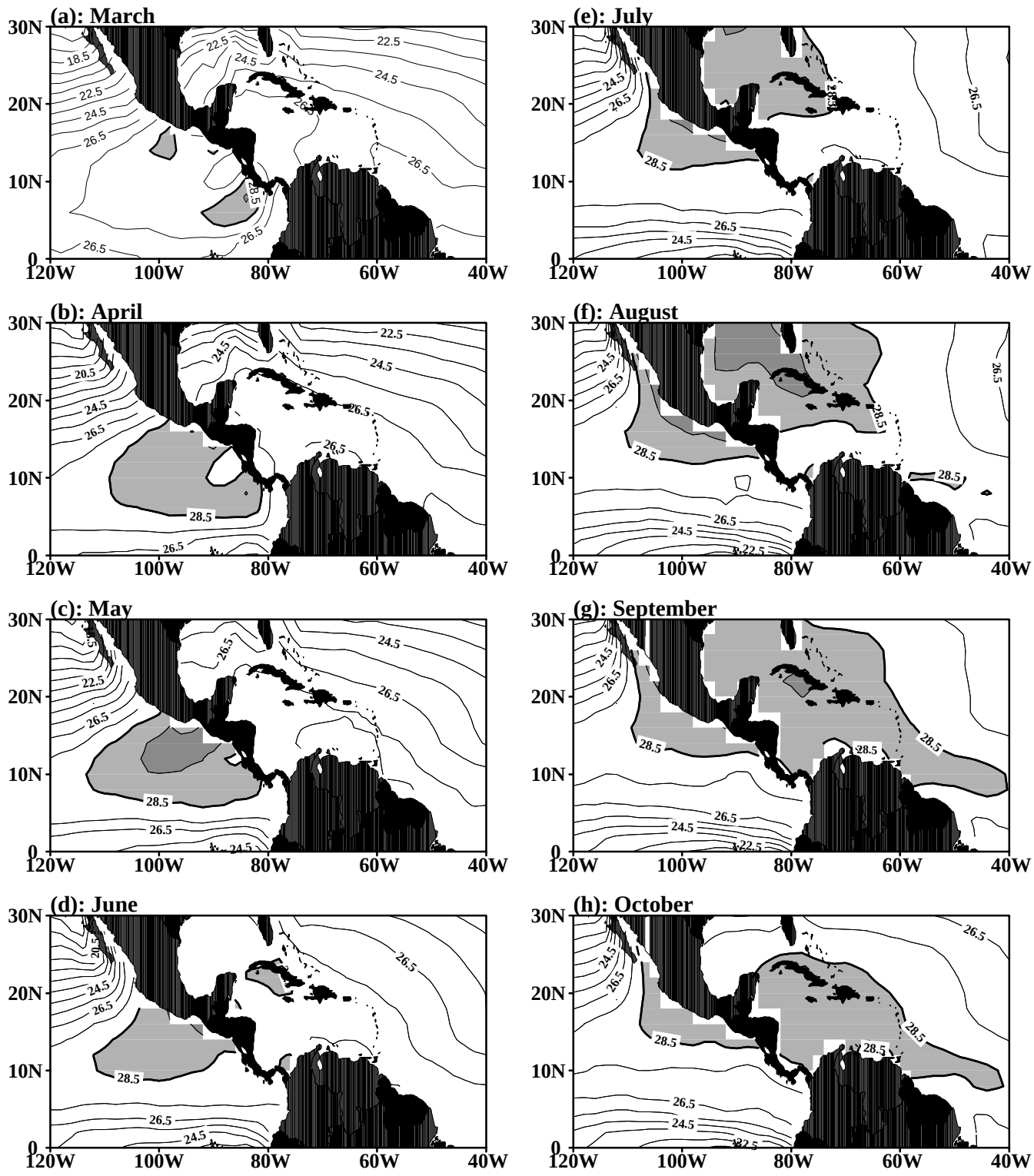

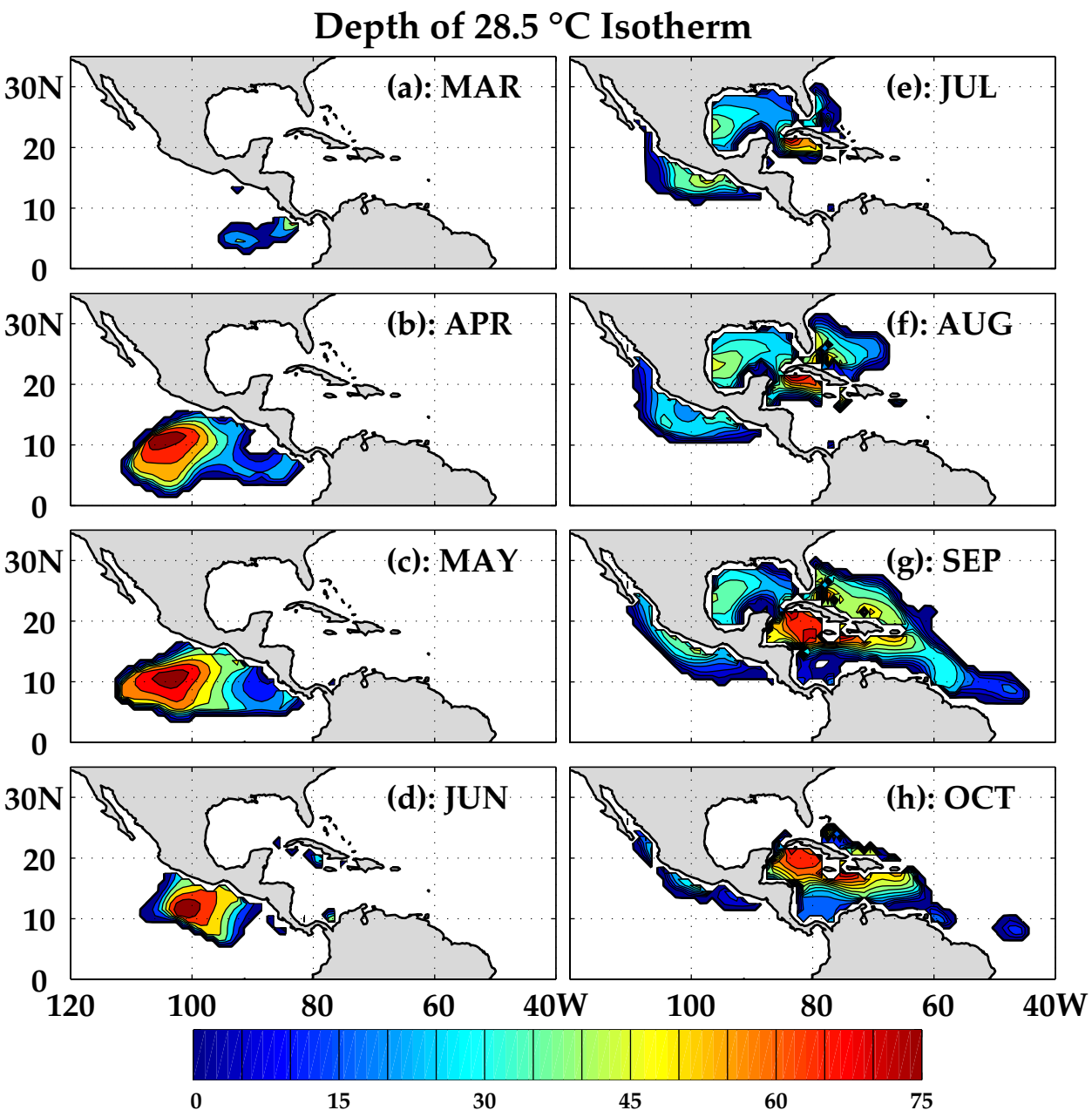
Depth of 28.5 °C Isotherm
(a): MAR
(b): APR
(c): MAY
(d): JUN
(e): JUL
(f): AUG
(g): SEP
(h): OCT
30N
20
10
0
120
100
80
60
40W
0
15
30
45
60
75

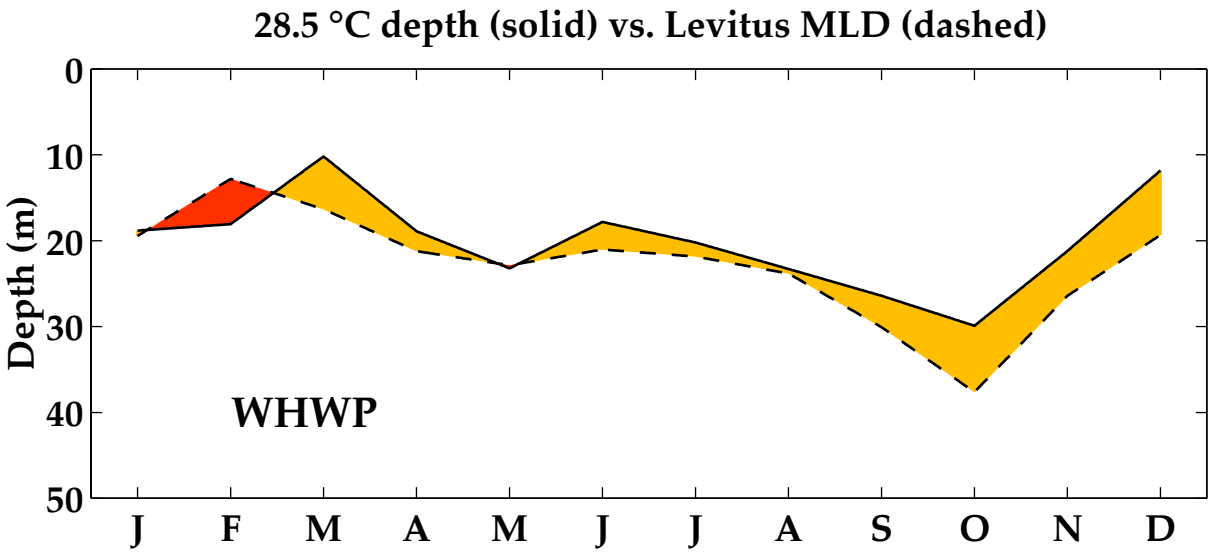
28.5 °C depth (solid) vs. Levitus MLD (dashed)
Depth (m)
0
10
20
30
40
50
J
F
M
A
M
J
J
A
S
O
N
D
WHWP

Western Hemisphere Warm Pool

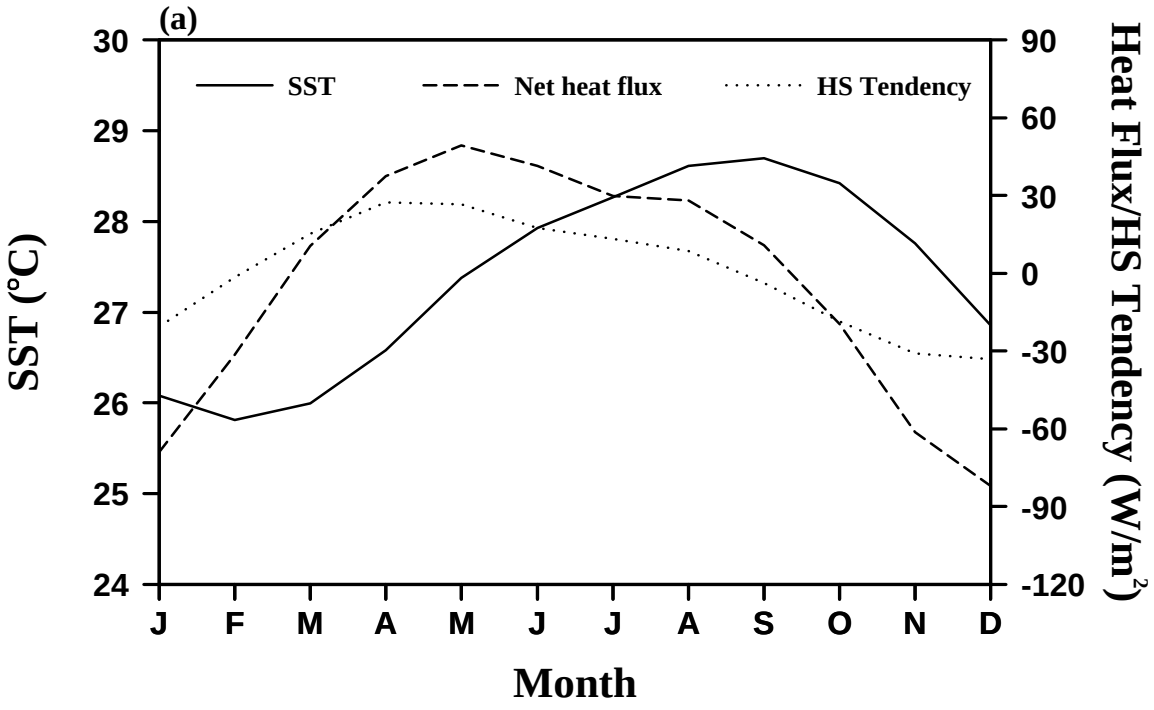

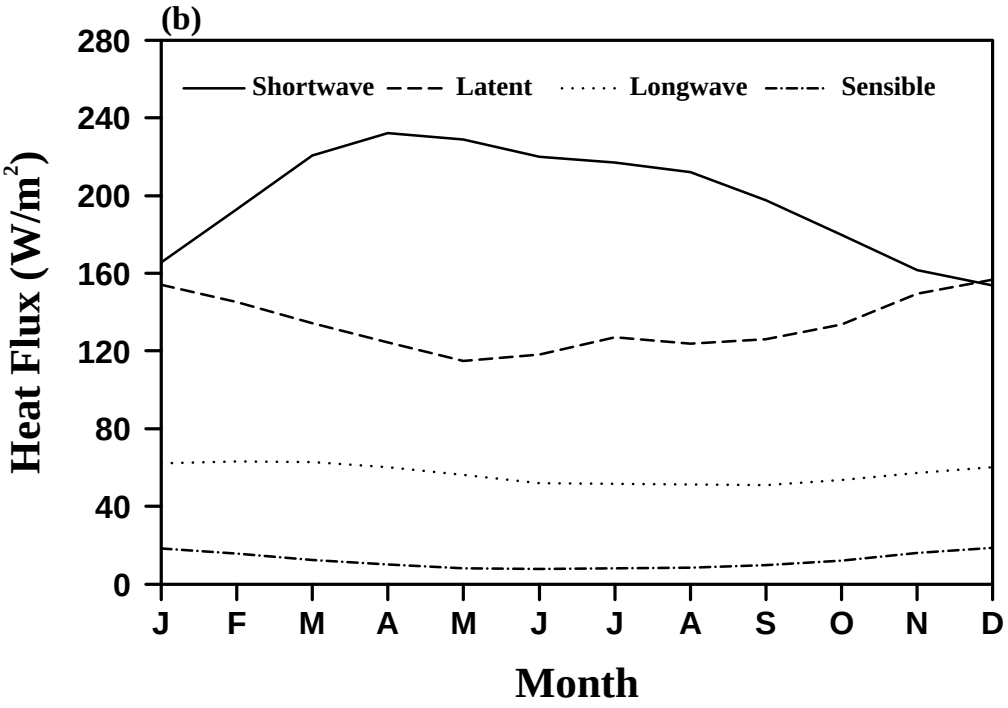

Climatologies (January)

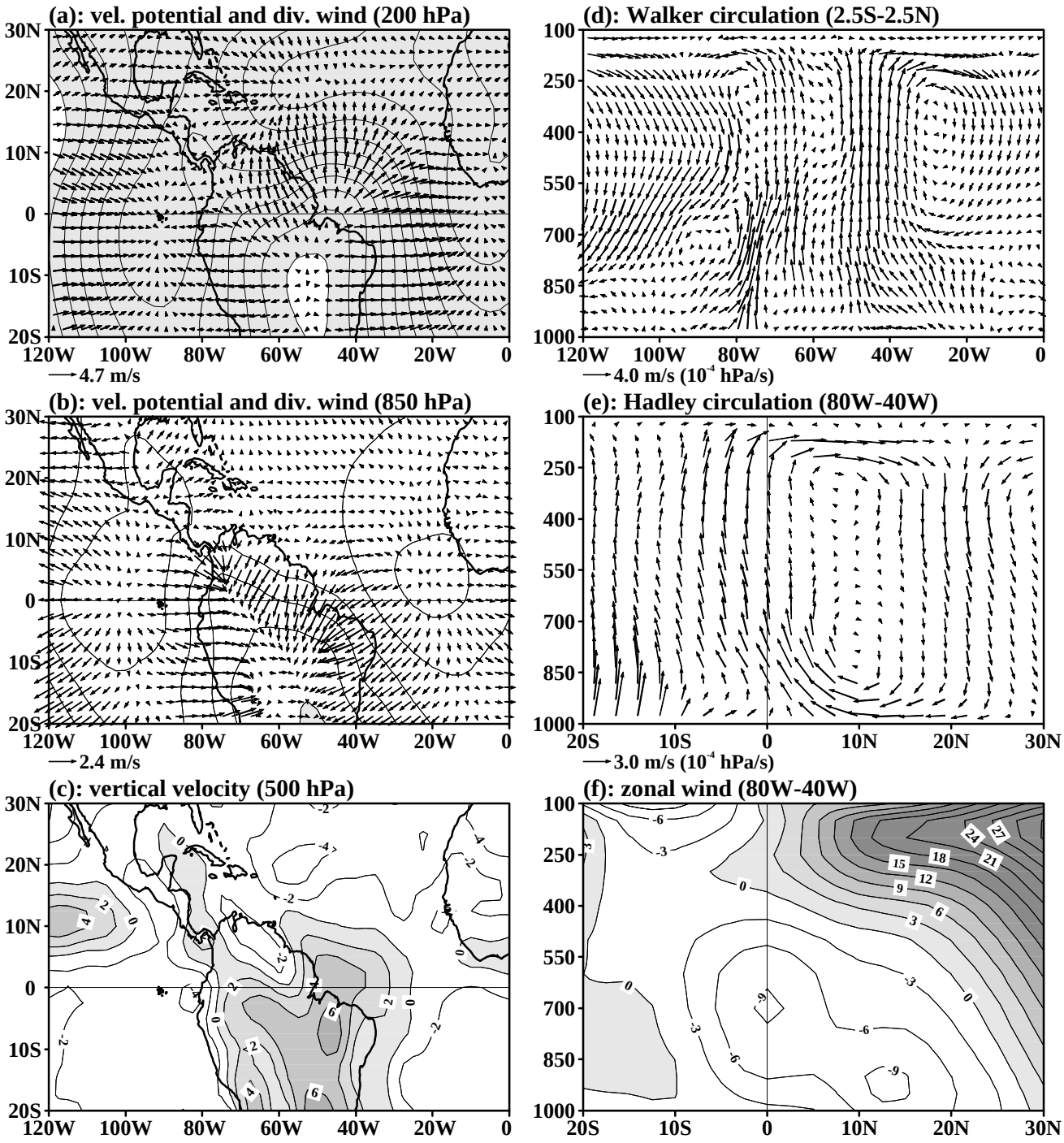

Climatologies (July)

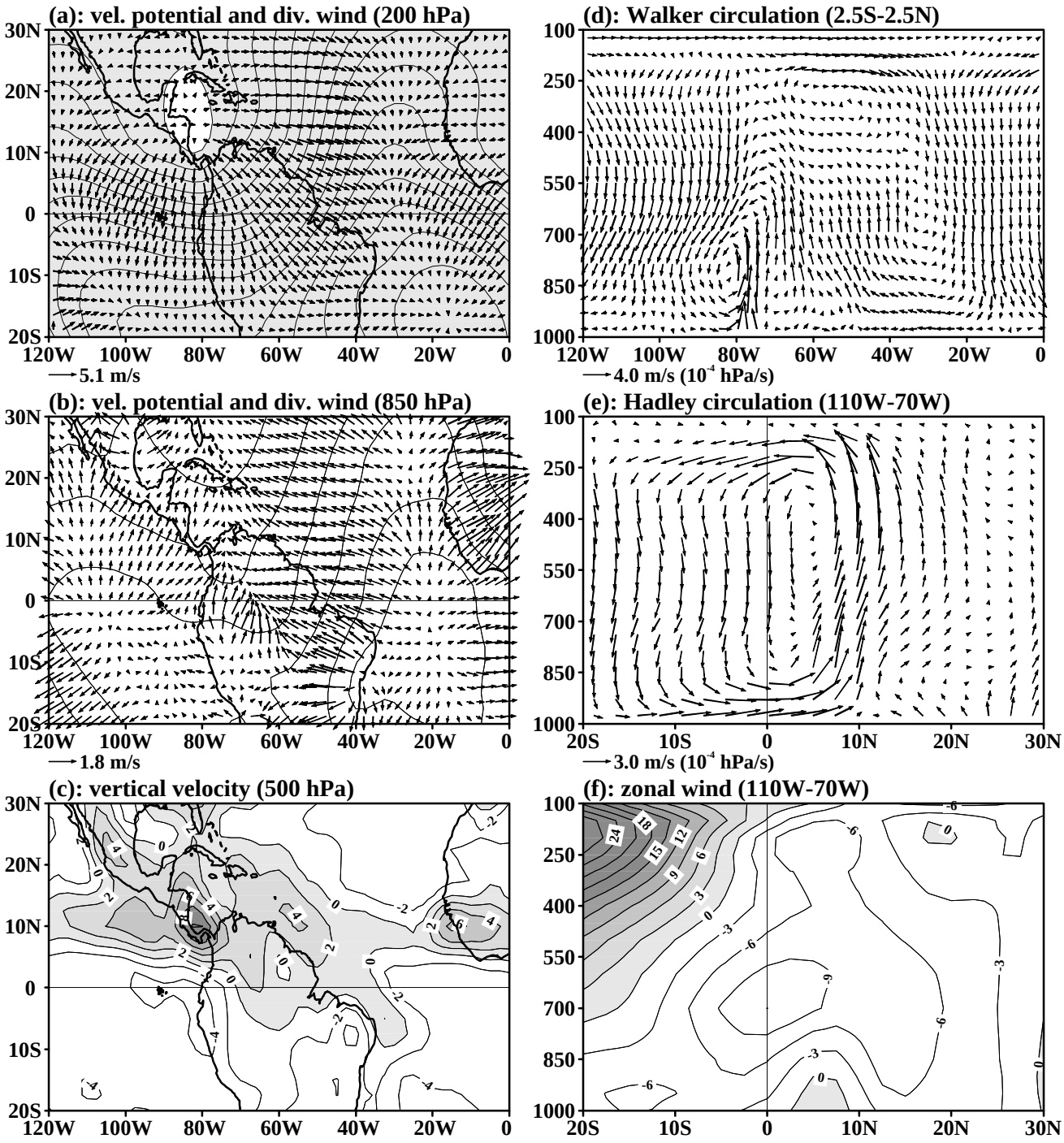

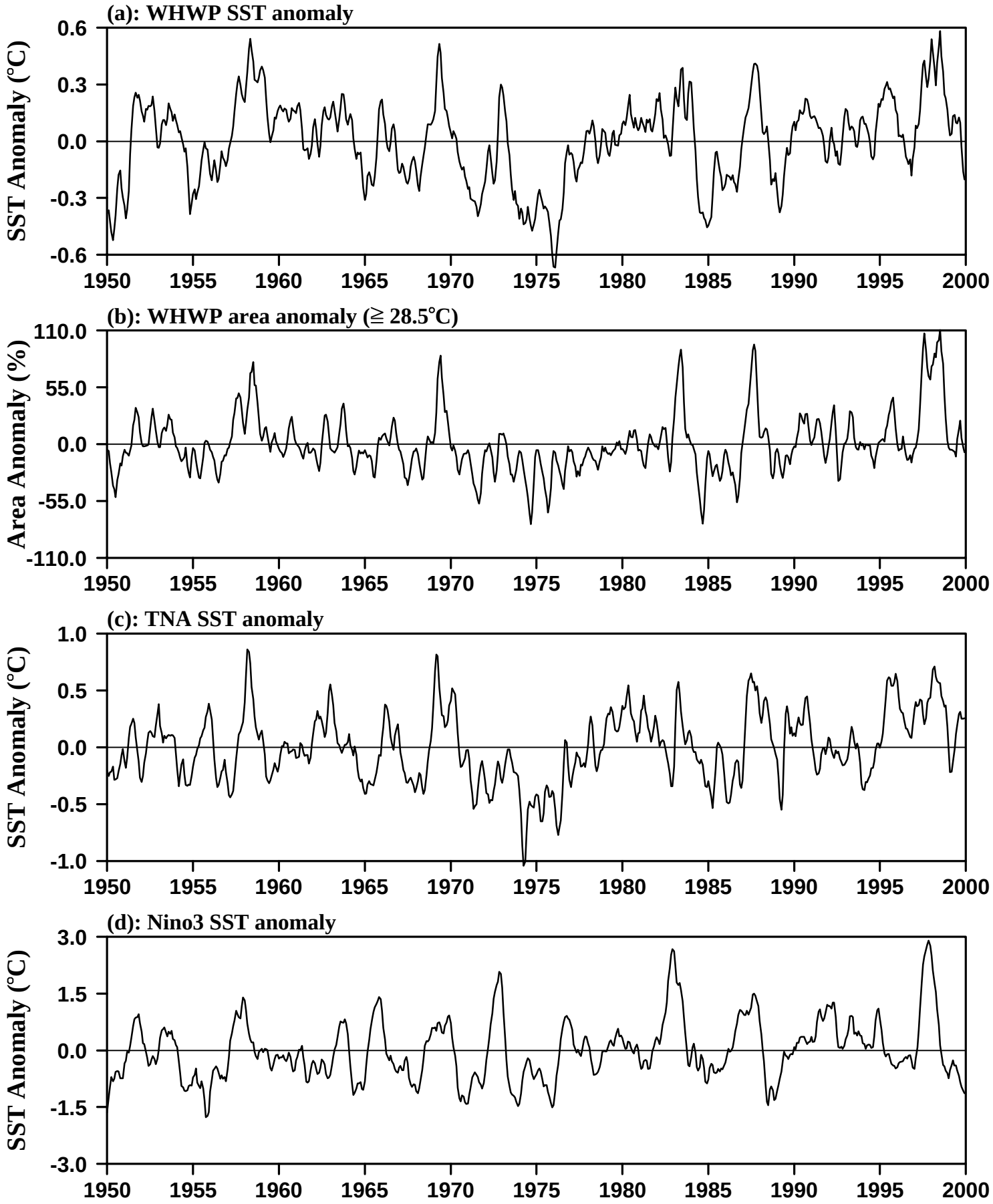
(a): WHWP SST anomaly
SST Anomaly (°C)
0.6
0.3
0.0
-0.3
-0.6
(b): WHWP area anomaly (≧ 28.5°C)
Area Anomaly (%)
110.0
55.0
0.0
-55.0
-110.0
(c): TNA SST anomaly
SST Anomaly (°C)
1.0
0.5
0.0
-0.5
-1.0
(d): Nino3 SST anomaly
SST Anomaly (°C)
3.0
1.5
0.0
-1.5
-3.0
1950
1955
1960
1965
1970
1975
1980
1985
1990
1995
2000

Composites of WHWP Warm Events

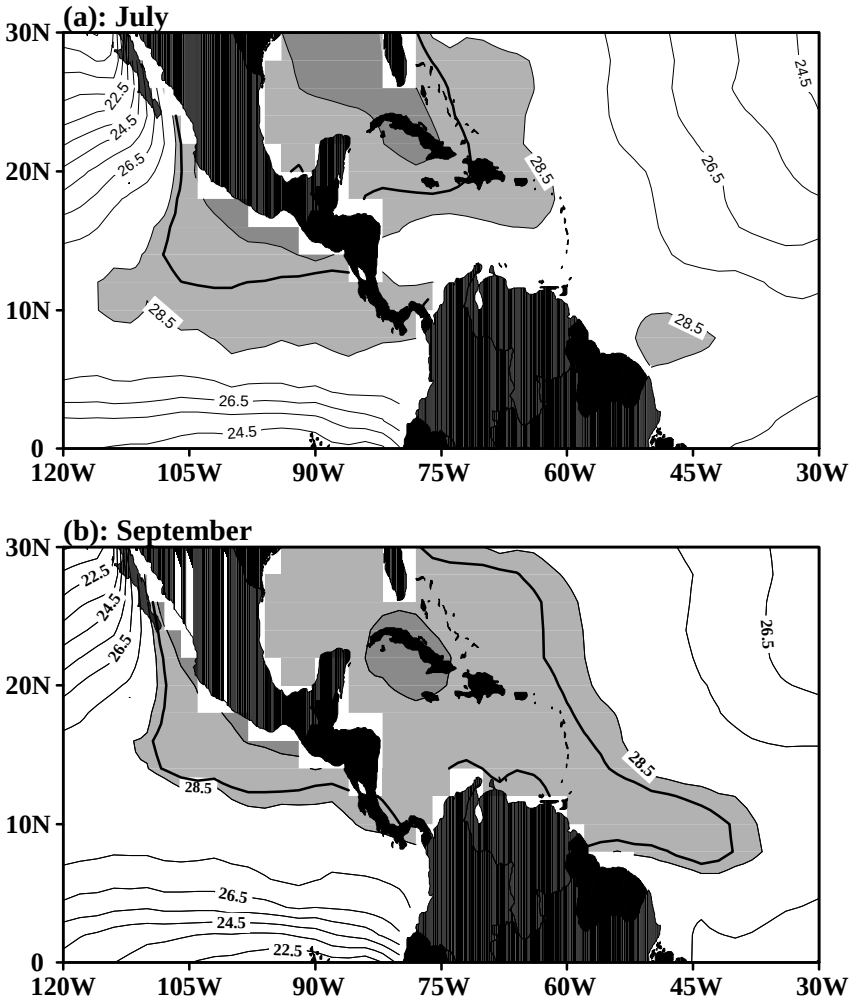

Anomalous Composites of WHWP Warm Events (Jan.)

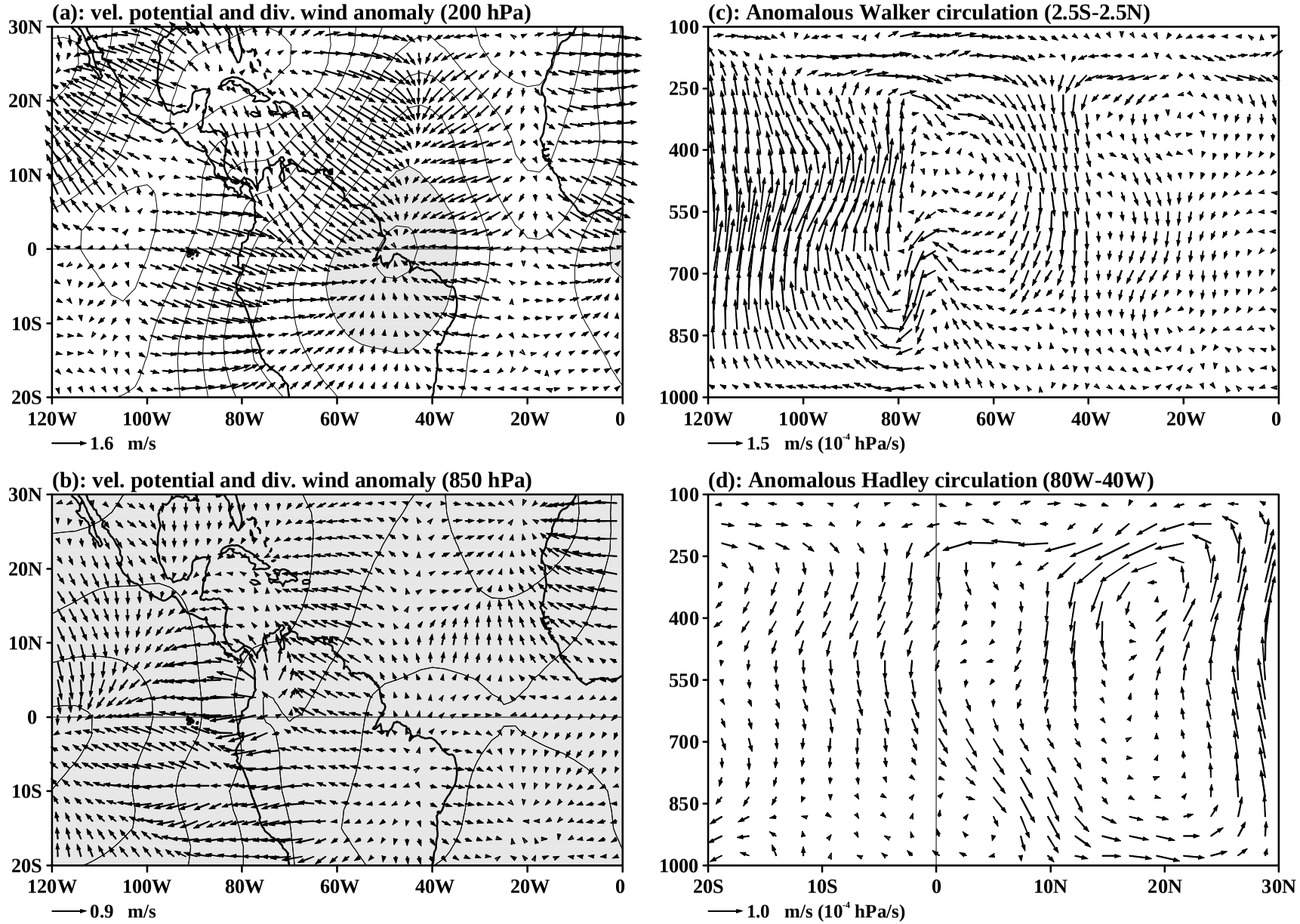

Anomalous Composites of WHWP Warm Events (Jul.)

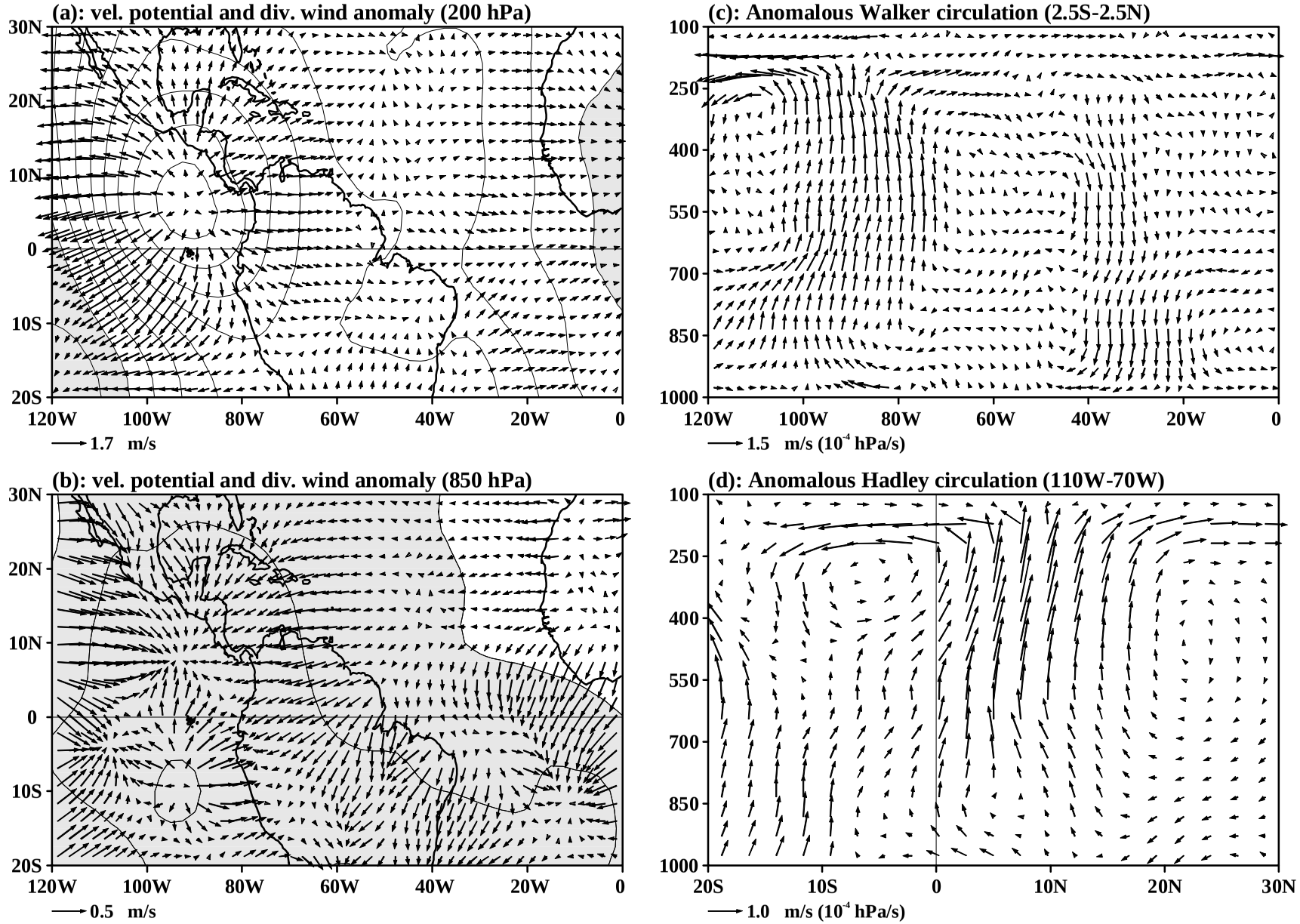

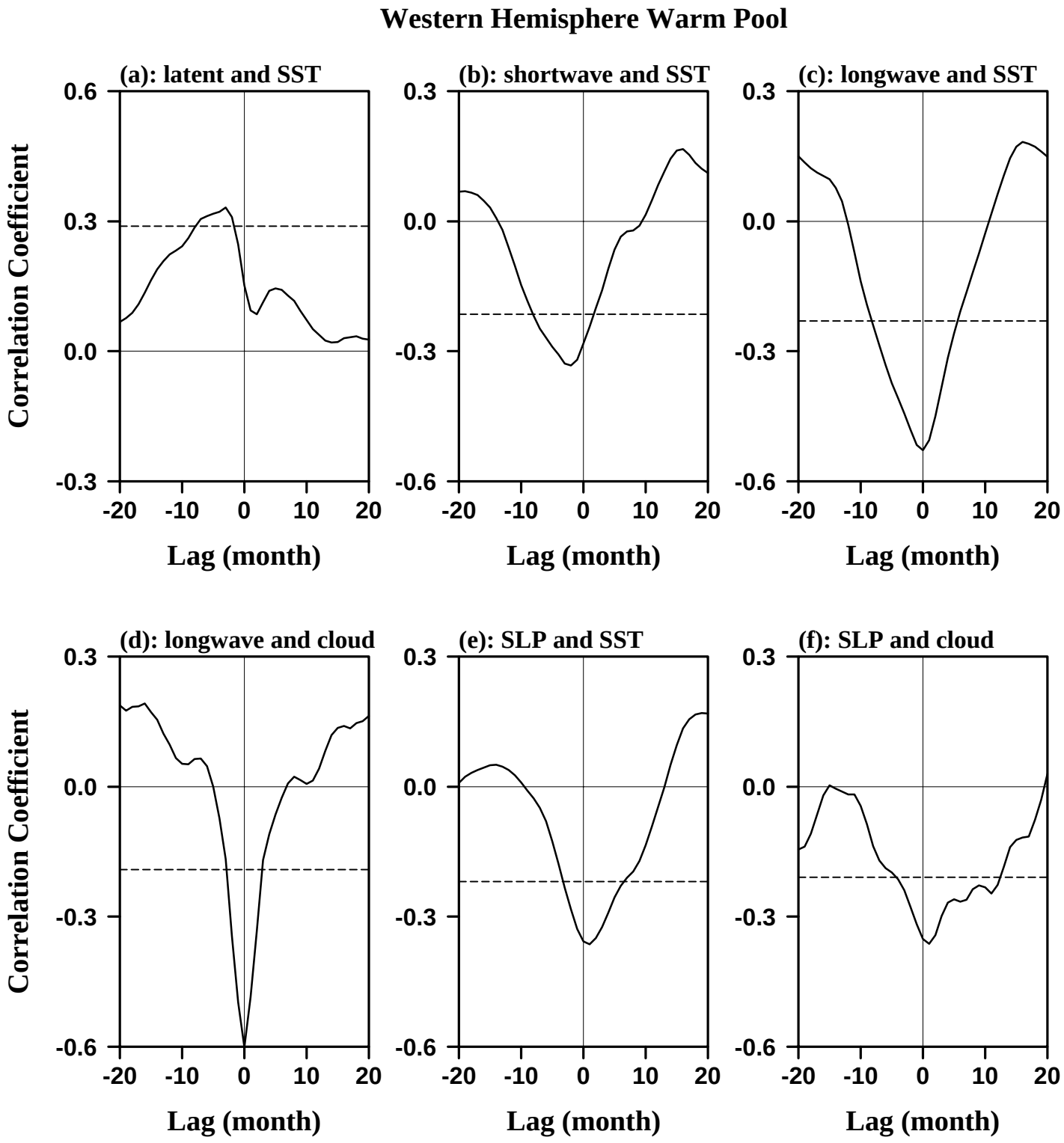
Western Hemisphere Warm Pool
(a): latent and SST
(b): shortwave and SST
(c): longwave and SST
(d): longwave and cloud
(e): SLP and SST
(f): SLP and cloud
Correlation Coefficient
Lag (month)
0.6
0.3
0.0
-0.3
-0.6
-20
-10
0
10
20

Composite of Longwave Radiation Anomaly

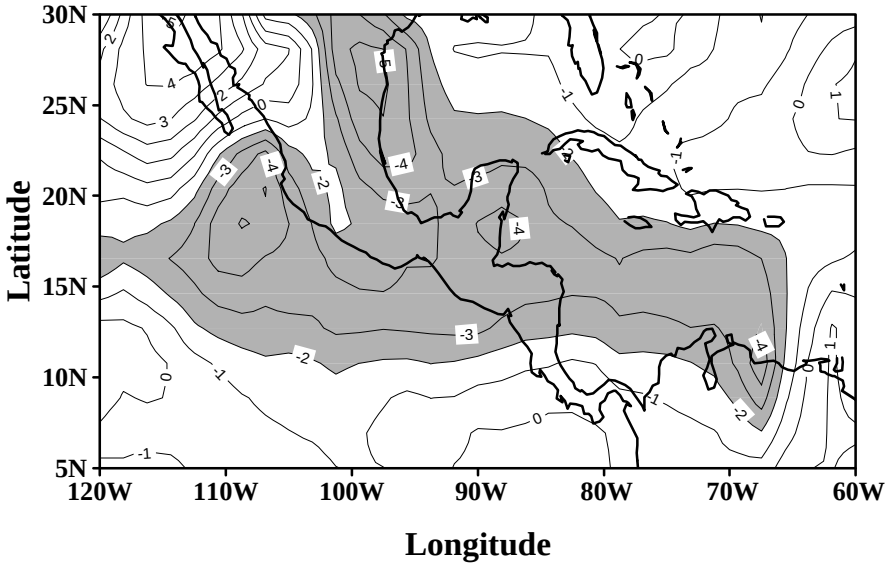

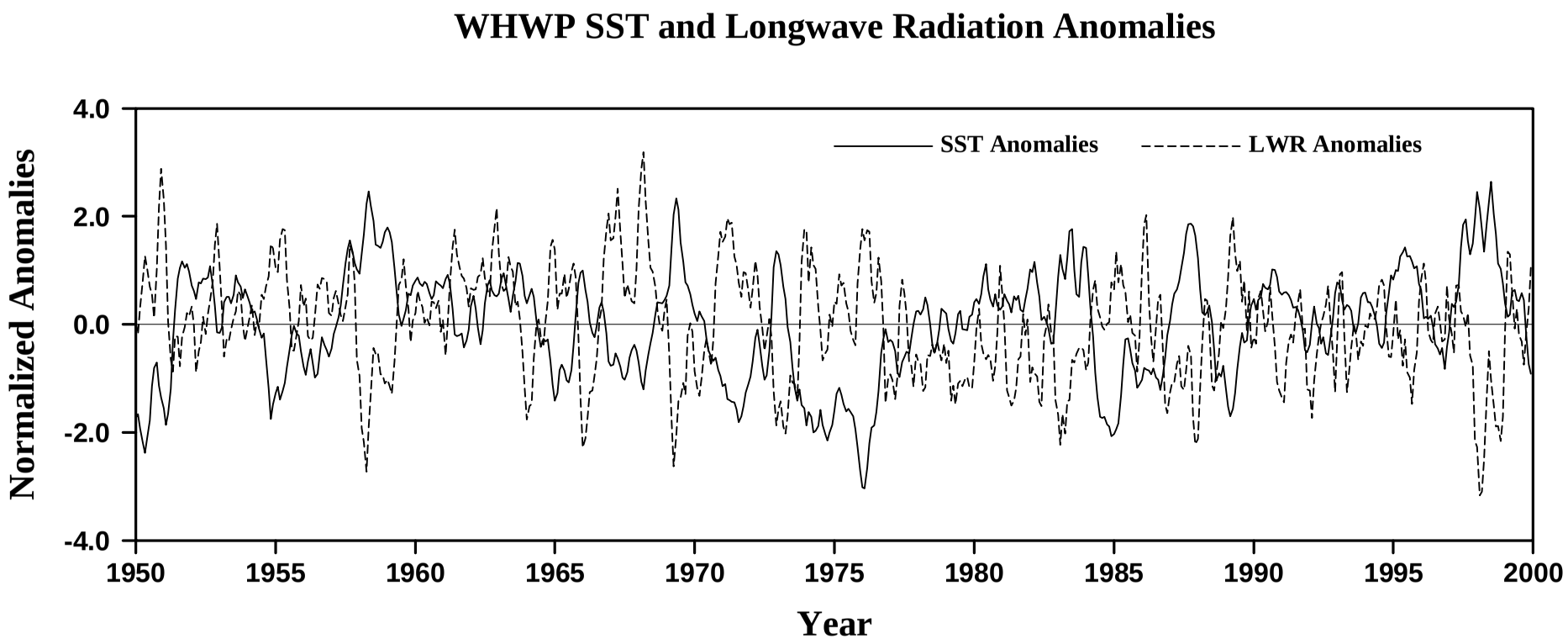
WHWP SST and Longwave Radiation Anomalies
SST Anomalies
LWR Anomalies
Normalized Anomalies
4.0
2.0
0.0
-2.0
-4.0
1950
1955
1960
1965
1970
1975
1980
1985
1990
1995
2000
Year